Acta Geophysica (2023) 71:1203–1224
https://doi.org/10.1007/s11600-022-00975-5

RESEARCH ARTICLE - APPLIED GEOPHYSICS

Interpretation of volcanic magnetic anomalies using differential search algorithm: case study from the Kula volcanic park, western Türkiye

Şenol Özyalın[1]

Received: 23 May 2022 / Accepted: 11 November 2022 / Published online: 5 December 2022

Abstract
A differential search algorithm (DSA) application, which is a metaheuristic inspired by nature, for total field aeromagnetic data caused by volcanoes over a 2D dipping dyke is presented. Inversion of the total magnetic anomalies was performed by adding the background level in addition to the parameters of the dyke model (e.g., dip angle, the depth to the top, half-width, the distance from the origin to the reference point, and amplitude coefficient), which are often tried to be estimated in the literature studies. In synthetic dyke models, the efficiency of the DSA in parameter estimation of theoretically generated magnetic anomalies that do not contain noise and contain random noise at different levels has been demonstrated. Firstly, in the synthetic dyke model, the efficiency of the DSA in parameter estimation of theoretically generated noise-free magnetic anomaly is demonstrated. Additionally, different levels of random noise were added to the same synthetic model anomaly to test the performance of the algorithm in case the data contained noise. The results of the inversion show that the model parameters estimated from the DSA agree well with the correct ones. This fit was also statistically checked by calculating the probability density function. In the real case, the inversion approach was then used to interpret five prominent total aeromagnetic anomalies over the well-known Kula volcanic field located in western Türkiye. The depths and widths of these magmatic bodies lying underneath these volcanic cones are about 450 m and 470 m, respectively.

Keywords Kula volcanic park · Aeromagnetic data · Differential search algorithm · Recent volcanic cones

Introduction

For many years, potential field methods, such as magnetic, gravity, and spontaneous potential (SP), have been frequently used to model and analyze subsurface geology (for example, mineral, ore, geothermal, oil, and natural gas explorations). Among these potential field methods, the magnetic survey is widely used to estimate geometric parameters of simple models (defined with depth, thickness, and shape) causing anomalies. Simple models for magnetic surveys can be in the form of a sphere, dyke, thin plate, or fault. Among these models, the dyke model is usually used in magnetic surveys (e.g., Srivastava and Agarwal 2010; Abdelrahman et al. 2012; Essa and El-Hussein 2017; Biswas et al. 2017).

The parameters of a buried two-dimensional (2D) inclined dyke structure are generally described with depth (D), half-width (W), the dip angle (δ), distance from the origin (x 0), and amplitude coefficient (P). Some or all of these parameters have been used to estimate using different evaluation methods, such as Fourier transforms (Bhimasankaram et al. 1978), integration nomograms (Atchuta Rao and Ram Babu 1981, Kara 1997), the midpoint (Murty 1985), Hilbert transform (Mohan et al. 1982; Ram Babu and Atchuta Rao 1991), automated numerical (Keating and Pilkington 2004), semi-automatic (Cooper 2012), and Euler deconvolution (Reid et al. 1990). In addition to these methods, we can also list modular neural-network inversion (Al-Garni 2015), non-linear constrained inversion (Beiki and Pedersen 2012), and derivative-based inversion methods (e.g., Gauss-Newton, steepest descent, and Levenberg-Marquardt; Marquardt 1963, Won 1981, Tarantola 2005, Pujol 2007, Essa and El-Hussein 2017).

Edited by Prof. Ali Gholami (ASSOCIATE EDITOR) / Prof. Gabriela Fernández Viejo (CO-EDITOR-IN-CHIEF).

✉ Şenol Özyalın
senol.ozyalin@deu.edu.tr

[1] Department of Geophysical Engineering, Engineering Faculty, Dokuz Eylul University, 35160 İzmir, Türkiye

The inversion process in the modeling of potential field data is an ill-posed and non-unique problem that requires appropriate constraints and additional priory knowledge for an accurate inverse solution (Li and Oldenburg 1996; Barbosa and Silva 1997). Traditionally, derivative-based inversion methods are widely used to estimate the parameters that require initial model parameters from geological information. The success of traditional inversion techniques depends on the accuracy of the geological prior information used to obtain a truthful solution. These traditional inversion methods have computationally fast convergence, which may fall into local minimums, instead of global minimums. This may diverge the solution from the real model with an incorrect initial guess selection of the parameters, which is due to searching for the optimum solution around the initial model. The inversion process continues iteratively until the error energy is minimized between the observed and predicted anomaly. Such shortcomings are the disadvantages of conventional inversion methods. However, the minimum-structure (Occam's) approach is widely used for the inversion of transient electromagnetic and direct current resistivity curves. It deals with the ill-posedness and non-uniqueness of the inverse problem very well. This method does not depend on the initial model. The advantage of the Occam algorithm over the traditional inversion algorithm Marquardt is that the inversion result is not dependent on the number of layers used and the initial model (Constable et al. 1987; Spies and Macnae 1997; Chen 1999; Farquharson 2008). In addition to these methods, enhanced local wavenumber (ELW) method was used in Canada and Egypt to determine the horizontal position and depth of the 2D dyke type magnetic structure without any prior knowledge (Salem et al. 2005). To determine the lateral boundaries of buried magnetic ancient remains, derivative methods such as the horizontal gradient magnitude (TF-hgm), the tilt angle horizontal gradient magnitude (THDR), the vertical gradient magnitude (TF-vgm), the balanced horizontal gradient magnitude (TDX), and finally the balanced horizontal gradient magnitude scaled by the analytic signal (TDXAS) were used (Stampolidis and Tsokas 2012). In the Eppelbaum 2015 study, quantitative interpretation of the magnetic data obtained on the thick bed model was performed.

Recent developments in computer technology have allowed the solution of complex geophysical problems with big datasets and provided a faster computation in the inversion process of subsurface modeling. This development also produced innovative metaheuristic inversion (MI) methods that are preferred to the traditional derivative-based inversion methods. MI methods, inspired by nature and modeling on the individual or social behavior developed by living beings to solve a particular problem, are very successful in solving numerical optimization problems. The basis of MI methods is based on the social swarm (herd, superorganism) model. Every living being in the swarm needs accommodation, nutrition to survive and reproduction to continue its generation (epoch). To meet these basic needs, they form groups by socializing and using the collective problem-solving skills of these groups. Socialization behaviors observed in living things (i.e., insects) are divided into three groups. They are Eusocial, parasocial and subsocial insects, respectively. Eusocial creatures are divided into three subgroups: overlap of generations (mothers live with their offspring for a period), cooperative brood care (females can care for offspring that do not belong to them), and reproductive division of labor (some members of a group leave more offspring than others). Honey bees, ants, termites, yellow jacket wasps and hornets can be given as examples of this group and are reproduced from a single queen their colonies have. Parasocial species are groups of sisters in which colonies consist of individuals of the same generation and often nest together. Although prosocial creatures have basic criteria such as cohabitation and reproduction, they do not raise their offspring together. Most of the living beings are in this group, and parasocial species live alone for most of their liveslife. Some neotropical orchid bees and Euglossa spp are examples of this species. The subsocial species is a subtype of the Parasocial species. Female insects in this group take care of their offspring for a long time to ensure the survival of the offspring. The European rove beetle and Bledius spectabilis are examples of this species (Otis 2004). Ants, termites and bees in the group of live colonies (e.g., swarm, held, superorganism) are produced by a single queen. During this reproduction, every living thing has its own genetic characteristics and they continue their generation at the end of natural selection. These living beings, which live in swarms, greatly improve their ability to overcome difficulties to survive and continue their generation. Numerical optimization algorithms are developed by observing the problem solving skills of these creatures based on swarm intelligence. Many researchers, for example, modeled the bees' foraging for food, ants' communication, and the cuckoo's joint care of their offspring, and developed inverse solution algorithms in reference to that living being's name.

Such well-known metaheuristic examples used for parameter estimation of geophysical anomalies are genetic algorithms (GA), differential evolution algorithm (DE), ant colony optimization (ACO), artificial bee colony (ABC), differential search algorithm (DSA), particle swarm optimization (PSO), cuckoo search algorithm (CSA) and simulated annealing (SA) algorithm. Specifically, these metaheuristic methods have been widely utilized by many researchers in gravity and magnetic modeling (Biswas and Acharya 2016; Ekinci et al. 2016, 2017, 2019, 2021; Balkaya et al. 2017; Biswas et al. 2017; Kaftan 2017; Essa and El-Hussein 2017; Gobashy et al. 2020; Di et al. 2020; Anderson et al. 2020).

The GA is an MI algorithm that uses an optimization method originating from the laws of genetics. The basic principles of genetic algorithms were first proposed by Holland (1975). The GA is generally an inversion method that models the evolution mechanism based on gene exchange in living beings. In this method, individuals of a population are shown as chromosomes and a series of genetic processes are applied. Each individual in the superorganism system has different genetic characteristics.

The DE is a population-based MI technique developed by Storn and Price (1995), based on genetic algorithms in terms of its operation and operators. Similarly, the DE and its derivatives are evolution-based algorithms. Crossover, mutation and selection operators in the GA are also used in the DE. This feature is the result of basic genetic processes. Unlike the GA, each operator is not applied sequentially to the entire population. Chromosomes are handled one by one and a new individual is obtained using the other three randomly selected chromosomes. By comparing the fitness of the new chromosome obtained using the previous chromosome, the new individual with better fitness is transferred to the next population. Thus, a selection operator is also used.

The basis of the ACO algorithm is based on the strategy of finding the shortest path between the ants' food sources and the colony while searching for food. As it is known, ants can secrete pheromone, which is a chemical substance used as a means of communication among themselves. Ants mark the way between the colony and the food source with the substance they secrete from their bodies. There is a relationship between the pheromone concentration released and the amount of food. In other words, an increase in the amount of secretion indicates an increase in the amount of food. From here, it is possible to say that the path with a more concentrated pheromone is the path to the food source with more food. The ACO algorithm is inspired by the behavior of real ant colonies. It was first introduced by Marco Dorigo (1992) and is based on the ants' strategy of finding the shortest path between the food source and the colony.

The ABC algorithm, developed by Karaboğa (2005), is an optimization algorithm created by mathematically modeling the unique intelligent behavior used by honey bee swarms when searching for food sources. Honey bees in nature share information such as the direction, distance and nectar amount of the food source they find through the dances they perform inside the hive. The bees that leave the hive in search of food initially make random exploration. Because of the small amount of food in the source they find, they begin to look for new sources or turn to other sources according to the information they receive from the bees. According to the type of work to be done in a natural bee colony, there is a division of labor among the bees and they can organize themselves. In the algorithm, a random solution is assumed to correspond to a nectar source. There are three types of bees in the ABC algorithm: employed bees, onlooker bees, and scout bees. Worker bees are tasked with bringing the food collected from predetermined sources to the hive. Another task is to share the location and quality information of the source they go with other bees in the hive. Onlooker bees wait in the hive and watch the worker bees. According to the information received by these bees, they are onlooker bees that turn to new sources. However, scout bees are bees that search for resources randomly.

The CSA is a population-based MI technique designed and developed by Yang and Deb (2009), inspired by the breeding behavior of cuckoos. The basis of the algorithm is brood parasitism. Cuckoos, acting like a parasite, lay eggs in the nests of other creatures other than their own. The cuckoo throws eggs with a high probability of hatching from the eggs belonging to the real nest owner creatures in the nest where they spawn. However, if the owner of the nest recognizes the egg of the cuckoo, it throws the egg or distributes it to rebuild the nest, or it shows the behavior of leaving the nest. However, if the owner of the nest cannot recognize the eggs, he sits on the eggs of the cuckoo like his own eggs and waits for the hatchlings to hatch. The advantage of cuckoos in this process is that their eggs hatch before the eggs of the nesting owner. The baby cuckoo tends to throw other eggs from the nest.

The PSO is a population-based optimization algorithm based on swarm intelligence developed by Kenedy and Eberhart (1995) by observing the social behavior of bird and fish swarms. PSO is based on social information sharing between individuals. Each individual is called a particle, and the population of particles is called a superorganism (swarm). It has been observed that the random movements of living beings acting in groups in a superorganism, in situations such as food and security, enable them to reach their goals more easily. The individuals forming the superorganism have individual and sürü memories. The basis of the PSO method is to use these memories to solve a problem. Individuals are thought to have an individual memory that uses the experiences gained from their random behavior. In solving such a problem, social memory is necessary so that the best solution that the superorganism can achieve, the individual who has not yet reached that solution, can benefit from it. By sharing information between individuals, a superorganism follows the individual with the best position in the superorganism while it is foraging or fleeing from a predator. While doing this, each individual updates their own position, their own speed and position according to the most successful individual by benefiting from their previous experience. This approach to velocity is random. Most of the time, individuals in the herd are in a better position in their new movements than in the previous position. The solution process of the problem continues until the goal is reached.

The search process is done by the number of generations (iteration, epoch) as in algorithms such as GA, DE.

The DSA inversion method is a swarm-intelligence based differential improvement algorithm. It is one of the promising techniques in solving complex numerical problems. DSA has only two control parameters and is not overly sensitive to the initial values of its control parameters. This increases the usability of DSA. Unlike Differential Evolution Algorithms, it contains only one distinct pattern different from the target pattern; that is, a candidate uses only two solutions to generate a solution. This allows DSA to work with a much smaller population sizes compared to very powerful algorithms such as DE/rand/1/bin (Civicioglu 2012). Classical PSO can be easily fitted to local solutions from time to time. Developed by Omran and Clerc (2011), PSO2011 is a complex PSO algorithm that contains different ideas from the results of researchers who have been using the PSO algorithm for years. It is not easily attached to local solutions like classical PSO, and its problem solving skills are very developed.

The MI method provides an advantage, over the traditional methods, such as allowing various search parameter space, whereas the parameters selected in the traditional methods must be close to the true solution. As in the DSA method, when using the meta-heuristics we mentioned above, a certain model (such as, sphere, cylinder) must be selected. In traditional derivative-based inverse solutions, it is necessary to take the derivative according to the unknown parameters. Difficulties may be encountered in deriving the complex relationships of some structures. An initial value is required for each parameter. In contrast, there is no obligation to assume a differentiation in meta-heuristics. The advantage of the method is to determine a large-parameter search space, not a single value for each parameter, when starting the solution. Perhaps a disadvantage of the method is the need for a countless number of forward modeling as the number of unknown parameters increases. By its nature, it increases in the number of iterations.

The DSA is an effective and novel swarm-based metaheuristic algorithm proposed by Civicioğlu (2012) for solving geocentric Cartesian to geodetic coordinate conversion problems. There are few studies in the literature using the DSA in geophysical surveys such as Rayleigh wave dispersion curve inversion for near-surface S-wave velocity profiles, inversion for parameter estimation from horizontal loop electromagnetic (HLEM) data, and, inverse modeling for interpreting magnetic anomalies, application of the DSA method to total magnetic anomalies collected from mining areas (Song et al. 2014; Alkan and Balkaya 2018; Balkaya and Kaftan 2021). However, this method has not been applied to the total magnetic anomalies of volcanic fields. But research on the determination of the structural features of Aegean region using magnetic anomalies is quite limited in the literature and should still consider structural features of the area in detail. Therefore, researchers have carried out different geophysical studies and used different evaluation methods to reveal general structure of the region. Some of these studies can be given as Ateş et al. (1999) emphasized in their study on aeromagnetic anomalies that the northwest of the region is more intensive than the south. Dolmaz et al. (2005) used magnetic data to reveal the Curie point depth and showed that CPD values ranged from 9 to 20 km. Bilim (2007) revealed the tectonic lines in the region. Bilim et al. (2016) computed the CPD and heat flow values for the Menderes Massif (MM). Erbek (2021) showed the location of the boundaries and the vertical-horizontal dimensions of the causative bodies in Aegean Region using magnetic data.

In this paper, the DSA application on total magnetic anomalies acquired in a volcanic area is demonstrated to characterize the form of dyke-shaped magnetic intrusions in the crust. Specifically, the applicability and efficiency of the technique have been examined. Additionally, an inversion was used to estimate the background level (C) along with the frequently used parameters of the dyke model (δ, H, W, D, and P). To do these, the DSA was: 1) applied to the inversion of noise-free total magnetic anomalies on a synthetically generated, inclined, thick-dyke model, 2) tested the performance of the algorithm on a noise-added total magnetic anomaly of the model, and 3) applied to total aeromagnetic anomalies acquired in the Kula volcanic area where is located at the NE of Aegean region of Türkiye (Fig. 1).

Kula volcanic geopark area

As Türkiye's first geopark, declared by UNESCO, is located in western Türkiye and is famous with extinct volcanoes, fairy chimneys, thermal water resources, and 80 small basaltic cinder cones associated with lava flows (Fig. 1). This area is surrounded by human and domesticated animal footprints dating from Pre-Neolithic times and hots antique settlements, which have been in use since Roman times. This volcanic area is in the northern part of Menderes massif, and it is a part of the geological young (Pleistocene and Holocene) volcano areas (Sözbilir 2002).

Geology and tectonic settings

The Kula volcanic region has a well-preserved record of the effects of crustal extension during Late Tertiary. This extension led to the structural juxtaposition of ductile-deformed mid-crustal rocks against brittle deformed supracrustal rocks in features known as the Menderes Metamorphic core complex, which includes gneiss, schist, and marble (Candan et al. 2001). The northern Menderes Massif is considered as a homogeneous area of low magnetization, with local

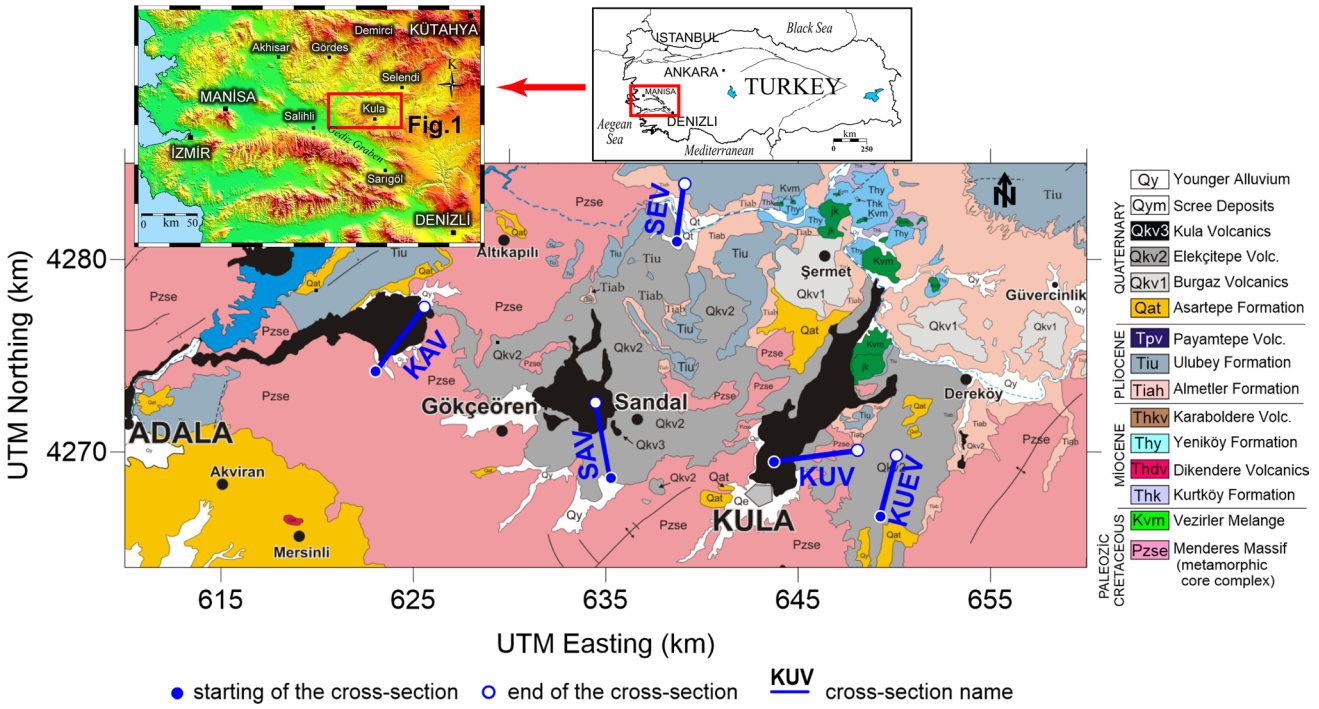

Fig. 1 Geological map of the Kula volcanic area (Tokçaer 2005)

anomalies related to the influence of interspersed magmatic bodies and shallow basins (Ozer and Polat 2017a). However, both the northern and western borders of Massif are the weak magnetic and ultramafic areas that are replaced by highly magnetized magmatic complexes (Gessner et al. 2016; Ozer and Polat 2017b).

The volcanic eruptions have been described in three phases; mass of basalt, numerous conical hills of scoriae, and ashes. These volcanoes are named Kula, Sandal, and Kaplan. The oldest Kula volcano is a plateau basalt with more than one main lava flows covering approximately 330–400 km^2. This plateau overlies the Late Miocene-Pliocene sedimentary succession. Meanwhile, the underlying, poorly indurated sediments underwent rapid erosion. Parts of the first-period plateau basalts were uplifted and partly eroded, while other parts were covered by younger lavas, tephra, and sediments. The youngest volcanic activity of the Kula area represents the beginning of second plateau formation (again the lava flows) along the main fault systems. The existence of a large volume of plateau basalts indicates rapid uplift of mantle material (Tokçaer et al. 2005).

Differential search algorithm (DSA)

The DSA is an effective population-based evolutionary metaheuristic that was proposed and developed by Civicioğlu (2012) to solve optimization problems in geodesy. The fundamental motivation of DSA is based on the migratory behavior of organisms moving away from a habitats with a low food supply capacity. This algorithm was mainly inspired by the migration of living beings that includes superorganisms such as many bird species, fire ants, honey bees, and monarch butterflies (Civicioğlu 2012). A superorganism (swarm) moves from a habitat with a low capacity for food resources to a greater food capacity. The individuals who make up the superorganism are called organisms. The movement of a superorganism can be described by a Brownian-like random-walk model (Civicioğlu 2012; Trianni et al. 2011). Throughout the year, the productivity of food areas in nature changes depending on seasonal climate changes, which decrease vital resources such as water resources and pastures. For this reason, many species show seasonal migration behavior throughout the year (Civicioğlu 2012). This migration enables living beings to move to food areas where more efficient natural resources are found (Şekercioğlu 2007). The migrating beings form a superorganism, containing many individuals, and test whether some randomly selected positions are temporarily suitable for a new habitat. If the new-fruitful habitat, named a stopover site, can meet the needs of the superorganism, which settles in the new region for a period, then repeats the same behavior toward more fruitful habitats. The meaning of stopover site in the algorithm corresponds to the best solution in each iteration, as in other MI methods. The basis of DSA method stems from the assumption that a population has random

solutions in a problem corresponding to an artificial superorganism migrating to the global minimum value. A summary of the inversion steps can be seen in the Appendix.

A superorganism consists of artificial organisms. The position of each individual in the artificial organism is randomly initiated. These positions are defined as X_i. Here, X_i, depending on the dimension of problem under consideration, is defined as x_{ij} and has dimension *Np x D, where* $i = \{1, 2, \ldots, Np\}$, $j = \{1, 2, \ldots, D\}$. Here, *Np* denotes the maximum number of populations and *D* depicts the size of optimization problem. In metaheuristic algorithms, the performance of algorithm depends on the control parameters and has a significant effect on the solution. The algorithm starts by specifying user-defined parameters (*Np* and *G*). Here, *G* denotes epoch (iteration, generation). In the algorithm, apart from the user-defined parameters control parameter, there are two control parameters (e.g., *p*1, *p*2) that describe the individual perturbation of members in finding more productive areas.

As in other population-based metaheuristic algorithms, an artificial organism can be randomly created within the user-specified lower and upper parameter limits by the following equation:

$$x_{i,j} = x_j^{\text{low}} + \text{rand}_{i,j} \times \left(x_j^{\text{up}} - x_j^{\text{low}} \right), \tag{1}$$

where $\text{rand}_{i,j}$ is a uniformly distributed random number between 0 and 1, x_j^{low} ($\text{low} = \{L_1, L_2, \ldots, L_D\}$) and x_j^{up} ($\text{up} = \{U_1, U_2, \ldots, U_D\}$) represents the lower and upper limits of *j*th dimension of respective problems.

The search process for finding the stopover site location is carried out by a Brownian-like random walk model. In this stage, the randomly chosen artificial organisms move toward the donor targets. At every stage of relocation, the locations of the individuals are located through random shuffling. The displacement size of superorganism is controlled by a scale value, which can be produced by gamma, normal, or lognormal random number generator and $donor = [X_{r1,\, G\text{random\_shuffling}}]$, where $r1 \in (1, 2, 3, \ldots, Np)$ and $r1 \neq i$ are the integers randomly determined.

The location of fertile stopover site is randomly generated from the artificial organisms in the current population and is described by a stopover vector $(s_{i,G})$. The stopover location can be identified with the following equation:

$$s_{i,G} = X_{i,G} + \text{scale} \times \left(\text{donor} - X_{i,G} \right). \tag{2}$$

In the algorithm, the elements of a stopover site that goes beyond the lower and upper limits determined in the search space are randomly distributed into the search space, as explained in Eq. (1). To conduct the search process that provides the determination of this stopover site, the trial vector can be defined by the equation given below:

$$S_{i,j,G}^{*} = \begin{cases} S_{i,j,G} \; if \begin{cases} \text{rand}_{i,j} = 0 \\ \text{rand}_{i,j} = 1 \end{cases} \\ X_{i,j,G} \end{cases}, \tag{3}$$

where $s^*_{i,\,j,G}$ indicates the trial vector of the *j*th particle in the *i*th dimension at the *G*th generation (epoch) and $\text{rand}_{i,j}$ is an integer number of either 0 or 1.

The process of determining the population that will survive in the next generation, defined by the following equation, is based on logical conditions and the selection process is made between a stopover site and the artificial organism population (Civicioglu 2012). According to the logical rule defined, if the trial vector provides an objective function equal to or smaller than that of the target vector, the location of the target vector is changed. Or else, the location of target vector within the habitat is preserved. DSA completes the selection process by applying the rule of greed and continues to search for more fruitful areas in the next generation.

$$X_{i,G+1} = \begin{cases} S_{i,G} \text{ if} \begin{cases} f\left(S_{i,G}^{*}\right) \leq f\left(X_{i,G}\right) \\ \text{otherwise} \end{cases} \\ X_{i,G} \end{cases}, \tag{4}$$

where $f(X_{i,G})$ and $f(s^*_{i,G})$ symbolize the currently best stopover site and the assessments of the newly explored stopover site. If the stopover site is not efficient enough in terms of food, in other words, until the global minimum is reached, the search process continues with Eq. 3, and otherwise, the search process is stopped. The objective function used in the selection process is defined by the following equation:

$$\text{RMS} = \sqrt{\frac{1}{N} \sum_{k=1}^{N} \left(d_k^{\text{obs}} - d_k^{\text{cal}} \right)^2}, \tag{5}$$

where RMS corresponds to the Root Mean Square Error, *N* is the number of data, d^{obs}, and d^{cal} denote the observed and predicted magnetic data, respectively, and *k* indicates the observations, where ($k = \{1, 2, \ldots, N\}$). The RMS is figured by the strategy which is considered as the misfit between the observed and predicted anomalies.

The basis of algorithm is based on the renewal of these two coefficients in a random process with a scale factor (SF) defined by the user in each generation. Civicioğlu (2012) defined the scale factor used in determining both control parameters from the results of test study to determine the most appropriate starting values as 0.3 ($p_1 = p_2 = SF \; x \; \text{rand}_{1,2}$, $SF = 0.3$), and accordingly, both control parameter range from 0 to 0.3. Here, rand_1 and rand_2 are two uniformly random numbers ranging from 0 to 1.

Alkan and Balkaya (2018) conducted a detailed parameter tuning study to determine these control parameters in the estimation of model parameters of HLEM anomalies and defined the scale factor used during the calculation of initial

values of control parameters ($p_1 = SF_1\ x\ rand_1$, $p_2 = SF_2\ x\ rand_2$, $SF_1 = 1$, and $SF_2 = 5$).

Balkaya and Kaftan (2021) used both initial values suggested above in the magnetic optimization problem. They compared to define whether there was an influence on the algorithm convergence rate. In the magnetic optimization problem, they revealed that the performance of DSA is quite good with the initial control parameters suggested by Alkan and Balkaya (2018). Starting from this point, the initial control parameters suggested by Alkan and Balkaya (2018) were used to estimate the parameters of magnetic anomalies.

Formulation of the magnetic anomaly

The 2D dyke model is generally used to evaluate magnetic anomalies. In this study, the magnetic anomaly value of thick, dipping dyke model defined by Venkata Raju (2003) at any point (x_i) on a profile on the surface can be defined by the following equation:

$$F(x_i) = P\left\{ \cos Q\left[\tan^{-1}\frac{x_i - D + W}{H} - \tan^{-1}\frac{x_i - D - W}{H}\right] + 0.5 * \sin Q \ln\left[\frac{(x_i - D + W)^2 + H^2}{(x_i - D - W)^2 + H^2}\right]\right\} + Mx_i + C, \quad (6)$$

where Q is the index parameter and P is the amplitude coefficient. H and W are the depth to the top of dyke and the half-width of dayk, respectively. D is the distance of origin (O) from the reference point (R). M and C denote a linear region of the slope and background levels, respectively. P and Q are given in Eqs. (7) and (8) for the total component (ΔT):

$$P = 2KT\beta(1 - \cos^2 I_o \sin^2\alpha)^{0.5}(1 - \cos^2 I_o \sin^2\alpha)^{0.5} \quad (7)$$

$$Q = I^1 + J^1 - \delta - 90. \quad (8)$$

The magnetic profile is along the x-axis, making an angle (α) from the magnetic north and the y-axis is along the strike of mass. I_0 and T are the inclination and intensity of Earth's magnetic fields, respectively. α and J_0 are the declination and inclination of the resulting magnetization (J). Here, α is the profile azimuth. The magnetic susceptibility contrast between the mass and medium is defined as I^1 and J^1, the effective inclination of induced and resultant field, respectively, where $\tan I^1 = \tan I_0/\cos\alpha$ and $\tan J^1 = \tan J_0/\cos\alpha$. The dip angle of thick dyke is denoted by δ and ranges between 0° and 180°. β is equal to sin (δ) for the dayk model and β is equal to cos (δ) for vertical fault. $J_0 = I_0$, $J^1 = I^1$ and $a = \alpha$ for induced magnetization.

Noise-free synthetic anomaly

A 2D dyke-shaped model was designed synthetically for the noise-free case to test the efficiency and success of the DSA method. The theoretical total magnetic anomaly was generated along the 1200 m profile length and with the sampling intervals of 25 m using the equation defined in Eq. 1. for a thick dyke, where $H = 100$ m; $W = 80$ m; $D = 650$ m; $\delta = 60°$; $C = 2500$ nT and $M = 0$. Other parameters in computing the anomaly, P, I_0 and α were set to 779 nT, 56°, and 0°, respectively.

DSA starts the optimization process by generating a random initial model using user-defined minimum and maximum limits of the estimation parameters. The evaluation process of magnetic anomaly is terminated using 40 independent solutions and a different initial model with the same parameter space boundaries each time. Finally, among these solution sets, the best parameter set with the lowest RMS value in the objective function is assigned as the best solution set. The population size (Np) is 100 individuals. A comparison of the predicted and observed magnetic anomalies without noise according to the best solution outcomes obtained from 40 independent solutions is shown in Fig. 2.

Actual and estimated parameter values are given in Fig. 2a. Figure 2b shows the variation of error energy according to the number of generations; on the other hand, Fig. 2c–h shows the variation of obtained model parameters in the number of generations. The red dashed lines in the figure represent the exact parameters and the black dashed lines indicate the half-standard deviation limits in epoch number. The black dashed lines show the spread of 100 organisms in each epoch for each model parameter. Although the spread was high at low epoch numbers, it was observed that the spread range was reduced at high epoch numbers. This means that the relevant model parameter is an indication of the increase in solution quality. Additionally, the epoch axis was defined as the logarithmic axes to better see the change in energy error and model parameters at lower epoch numbers. Statistical values (worst, mean, std) of the obtained parameters and RMS results are presented in detail in Table 1. Moreover, Table 1 illustrates the best-estimated model parameters of DSA in different epochs and the search space bounds used during optimization. As shown in Table 1 and Fig. 2, it is observed that all model parameter values stabilize after approximately 50 generations. Although the RMS value was 293 in the initial solution, it was 0.3 in 50 generations and very close to zero in the last generation. According to the change in RMS error values, increasing the epoch size to more than 50 epochs does not have much effect on the solution.

One method for the statistical interpretation of obtained data is also a relative frequency histogram. The relative

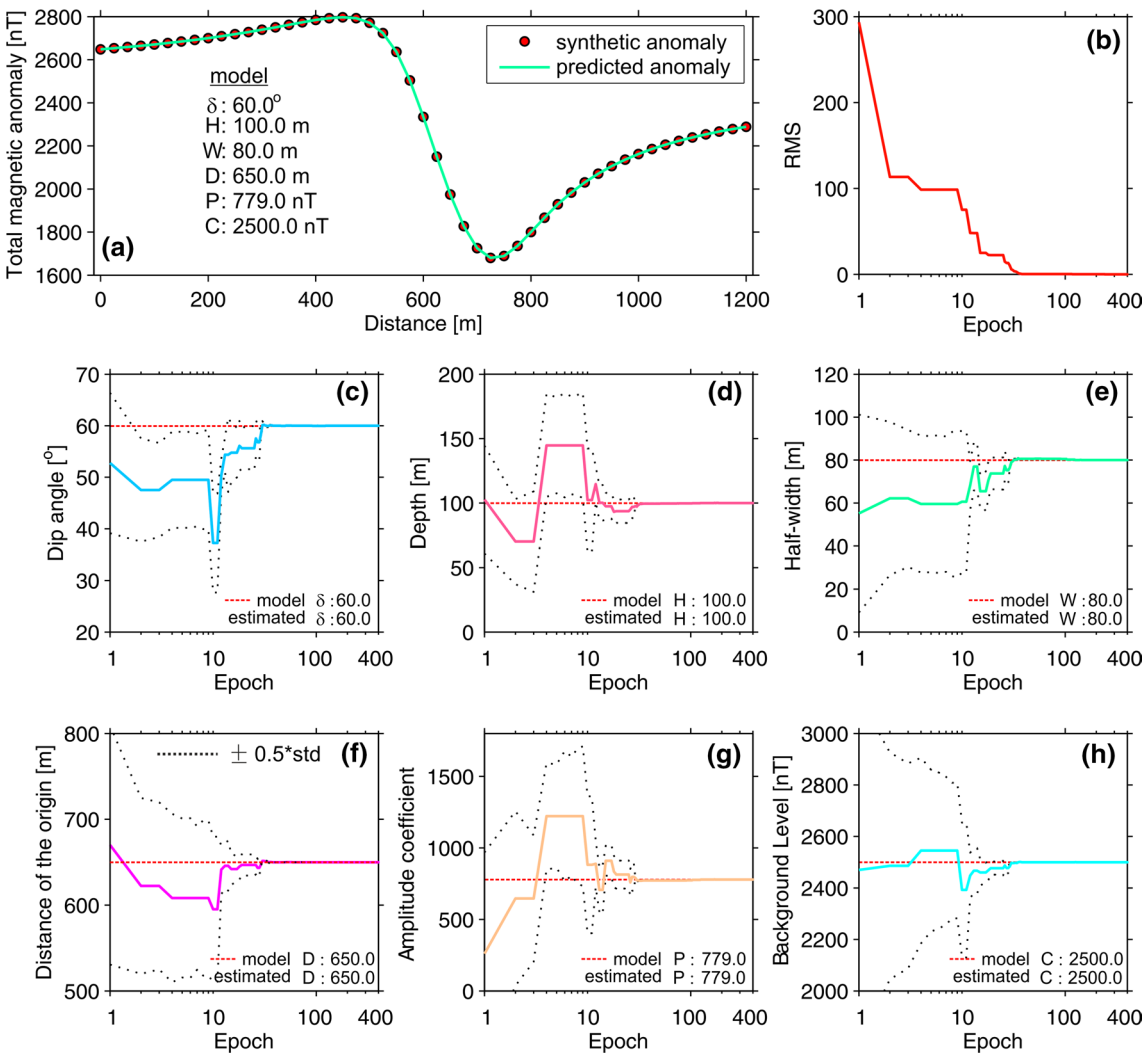

Fig. 2 **a** The comparison of the theoretical and predicted anomalies, **b** Changes in the error energy with the epoch, and **c–h** present changing of model parameters at each epoch

Table 1 Results of the DSA both noise-free and noisy synthetic total magnetic anomaly for thick dyke

Model parameters	δ [°]	H [m]	W [m]	D [m]	P [nT]	C [nT]	RMS
True model	60	100	80	650	779	2500	
Search spaces	0:90	1:300	1:300	100:1100	50:5000	50:5000	
Noise-free case	60.00	100.00	80.00	650.00	779.00	2500.00	0.00
Noisy case with std of ± 10 nT	59.51	99.30	77.74	648.70	792.02	2497.83	9.19
Noisy case with std of ± 20 nT	59.50	98.83	82.62	647.43	760.74	2489.54	19.37
Noisy case with std of ± 30 nT	58.96	98.39	69.99	652.57	865.89	2489.33	26.59
Percent relative error							
Noisy case with std of ± 10 nT	0.82	0.70	2.83	0.20	1.67	0.09	
Noisy case with std of ± 20 nT	0.83	1.17	3.28	0.24	2.34	0.42	
Noisy case with std of ± 30 nT	1.73	1.61	12.51	0.40	11.15	0.43	

frequency distribution, also called probability histograms, is important for the statistical representation of certain outcomes occurring within a given population and the number of times they occur. Relative frequency distributions of all parameter results belonging to the noise-free synthetic model obtained from the DSA are denoted in

Fig. 3. To prepare these histograms, first, the best solution among 40 independent solutions was determined. A data set (400 × 100) containing the solutions of 100 organisms over 400 epochs of each model parameter in the best solution was used. It is important to prepare the frequency distribution for each model parameter. This is because it gives us valuable information about the quality of solution and is used in the interpretation phase. The histograms prepared for each parameter are displayed between the minimum and maximum limits of parameters, and the best real parameter values obtained from the solution are also shown on the histograms. The concentration of parameter estimates in a narrow area in histograms indicates a good resolution. In contrast, it shows that the margin of error increases in case the boundaries of field are widened. In Figs. 3a, d, f, we can see that the relative frequency distributions of δ, D, and C are symmetrical. It is clearly observed that the dip angle is grouped at 60 degrees with 85%, the distance of origin at 650 m with 90%, and finally at 2500 m with 80% of the background level. We can also see that the distribution of W spreads slightly to the left, while the distribution of amplitude coefficient distribution is quite strong and spreads widely to the right. Therefore, the half-width of dyke has a comparatively wider range compared with other parameters. In other words, the uncertainty in the solution of half-width (W) and amplitude coefficient (P) of dyke is greater.

Although we obtained successful dyke parameters such as δ, H, W, D, P, and C, probability density function (PDF) was also applied using dyke parameters with best solutions from 40 separate runs to statistically test the reliability of the solution.

The statistical function of the PDF is expressed with the following relation and the normal distribution is calculated using the mean and standard values:

$$\mathrm{PDF}(x) = \frac{1}{\sigma\sqrt{2\pi}} e^{-(x-\mu)^2/2\sigma^2}, \tag{9}$$

where μ and σ show mean value and standard deviations (std), respectively. If x is discrete data, the sum must be $f(x) = 1$ for all values for which x is defined, otherwise, if x is continuous, the integral of $f(x)$ must be one for the interval where x is defined, that is, under the curve, the whole area is equal to one. Figure 4 shows the confidence interval limits of mean parameter values with a probability of 95%. The blue line on the figure shows the probability density function with a probability of 95%. The red-blue line and the dashed black line represent the mean parameter value and the best parameter value, respectively. Finally, the colored rectangle shapes demonstrate confidence interval levels with a probability of 95% for the mean parameter value. The meaning of density distribution function is that the lower the std values, the narrower the parameter range. It is clearly observed that the PDF distribution calculated for each parameter obtained from the best solution has a very low std. Therefore, the solution is placed in a narrow area, and the parameter value remains in the safe region. It clearly shows that the parameter estimates obtained by DSA are within confidence intervals without any uncertainty.

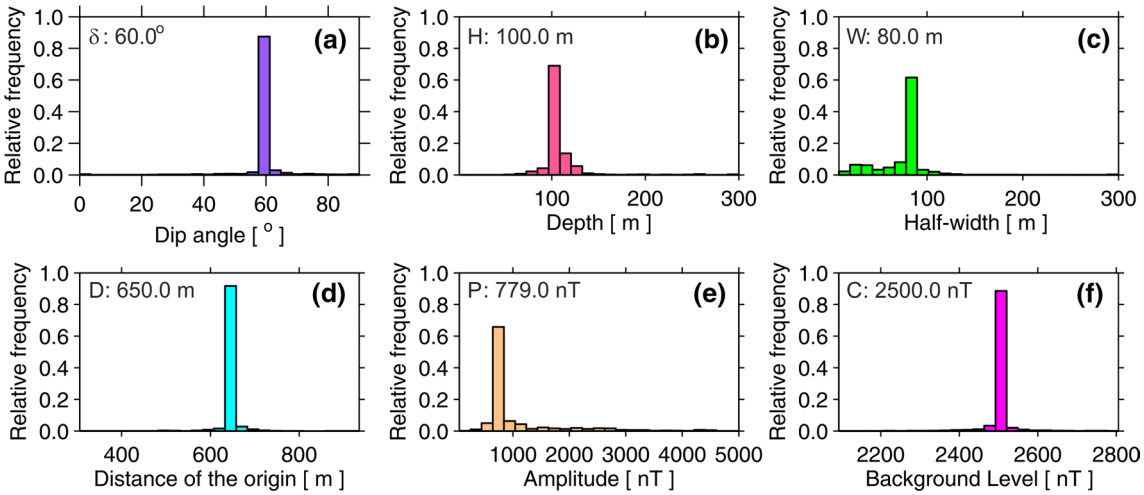

Fig. 3 Relative frequency distributions produced by using a solution set containing model parameters obtained the best runs of the DSA belong to the noise-free case of the theoretical model

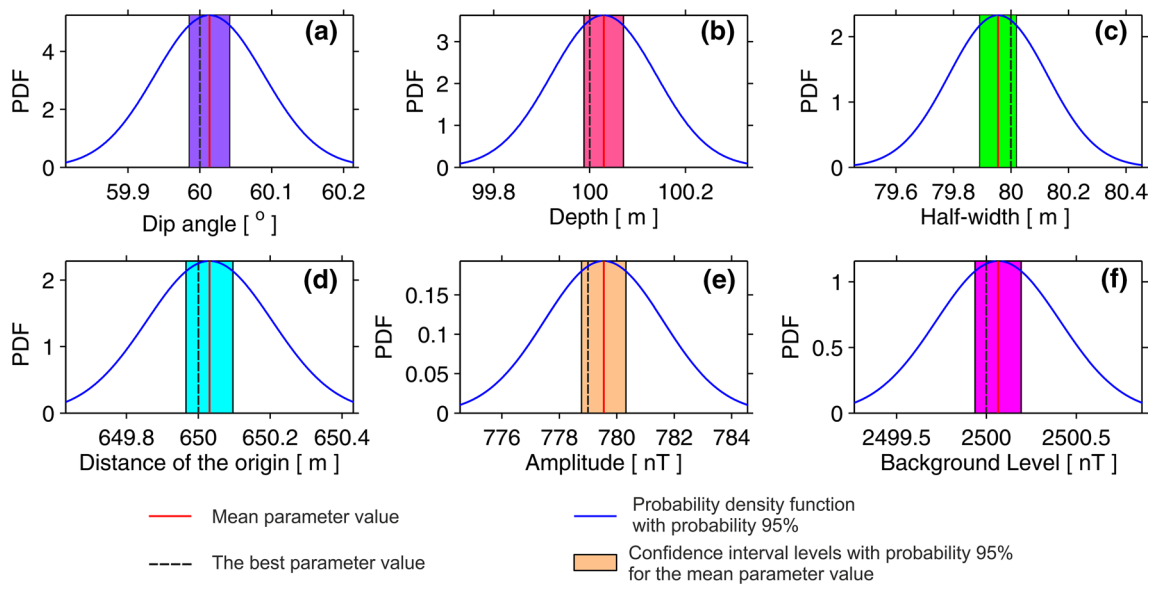

Fig. 4 Figure denotes PDF analyses of the best model parameter values obtained in 40 separate runs in case noise-free magnetic data example

Noisy synthetic anomaly

To test the performance of algorithm on data containing noise, we added random normally distributed noise with zero mean and with a std of ± 10, ± 20, ± 30 nT, respectively, onto the magnetic anomaly produced using the model parameters of dyke-shaped body shown in Fig. 5. Figure 5a shows the theoretically generated magnetic anomalies without noise (red-filled circles) and with added noise (e.g., red line, green line, blue line) having a std of ± 10, ± 20, ± 30 nT, respectively. Figure 5b shows the variation of error energy according to the number of generations and Fig. 5c–h presents the variation of obtained model parameters. As in the noise-free synthetic models, the cross section of which is shown in Fig. 2, in the noisy synthetic model, the length of profile with 61 measurement points is 1200 m and the sampling interval is 20 m.

In Table 1, a comparison of the parameter results obtained from the DSA for the theoretically generated noise-free and magnetic anomaly cases, including the randomly generated noise levels for different standard deviation values is given. In the case of noise-free anomaly evaluation, the model parameters obtained from DSA were determined to $\delta = 60°$, $H = 100$ m, $W = 80$ m, $D = 650$ m, $P = 779$ nT, and $C = 2500$ nT with an error value of RMS = 0.00001. In the case of anomaly assessment involving noise (only for std of ± 30 nT), the model parameters were determined as $\delta = 58.96°$, $H = 98.39$ m, $W = 69.99$ m, $D = 650.57$ m, $P = 865.89$ nT, and $C = 2490.33$ nT with an error value of RMS = 26.59. Also, the parameter results for other noise-containing model cases are detailed in Table 1. Additionally, true and estimated model parameters are indicated on each subplot. As shown in Table 1, it is clearly observed that the RMS error values increase as the noise level increases.

Additionally, the amount of error in parameter values of dyke (e.g., H, W, C, …) obtained from the DSA solution of synthetic models containing noise was calculated. The amount of error in the parameters is the difference between the actual value of model and its predicted value. This error can be expressed as the absolute error (the numerical amount of difference between the true value and the predicted value) or relative error (absolute error divided by the true value). Usually, percentage relative error is used instead of relative error, which is the relative error multiplied by 100. As can be seen from the percent relative error rates for the std of ± 30 nT given at the bottom of Table 1, the largest error values are observed in the amplitude coefficient (P) and half-width (W) of the dyke. While the amplitude coefficient and half-width error values are 11.15% and 12.51%, respectively, they are below 2% in other variables (e.g., δ, H, D, C). While the lower rate of noise did not affect the model parameter solutions, higher rates of noise, particularly over std of 20 nT percent, significantly affected it. According to the change in the objective function values corresponding to the RMS error values shown in Fig. 5b, the solution shows a rapid convergence for noisy synthetic data after the 100th epoch. In other words, increasing the epoch size to more than 100 epochs does not have much effect on the solution. In the application, Emax was fixed at 100 epochs.

The evaluation process of magnetic anomaly is applied 40 times using a different initial model for each run. Among the results, the PDF distributions with a 95% confidence interval for each variable of the best model solution with a minimum RMS error value are shown in Fig. 6. According to the PDF

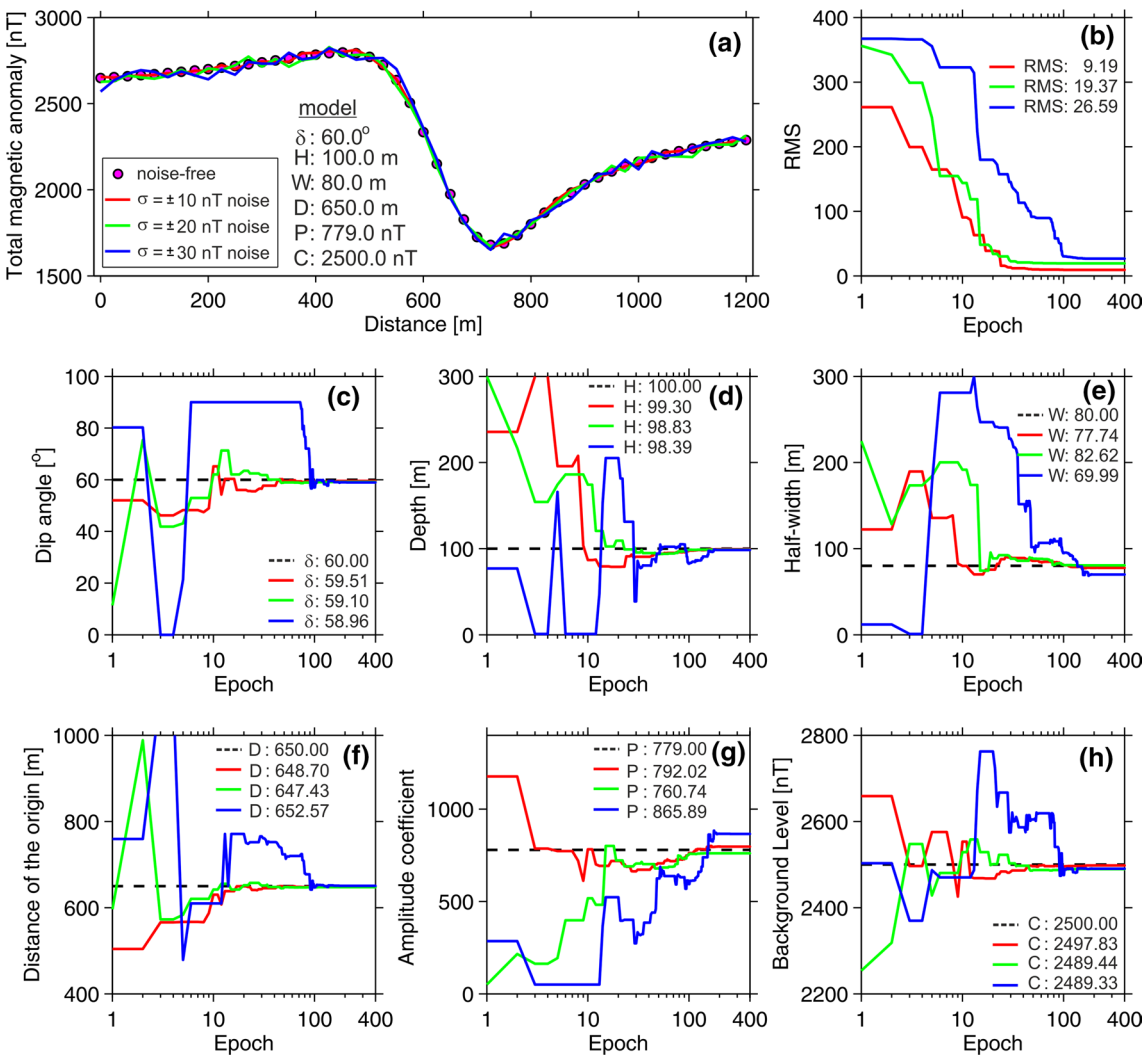

Fig. 5 **a** The comparison of the theoretical and predicted anomalies, **b** Changes in the error energy with the epoch, and **c–h** present changing of model parameters at each epoch

distributions shown in Fig. 6, we observe that the solution of each variable is within the confidence interval. In Fig. 6d, it is clearly observed that the value of the distance of origin is close to the mean value, while the remaining variables are close to the confidence interval limits.

The aeromagnetic data of the Kula region

The aeromagnetic anomaly map which was used in the context of study was adopted from (MTA 1962). The International Geomagnetic Reference Field (IGRF) values were eliminated from the data used in this study. It was flown at a terrain clearance of 150 m with the flight lines at about 1 km intervals (Fig. 7a). One of the most obvious aeromagnetic anomalies in western Türkiye is related to the Kula volcanics. Aeromagnetic anomalies are very distinctive and these are easily correlated with the basaltic rocks of region having magnitudes up to 3000 nT. It can be distinguished that the positive anomaly enclosures are over the first and second phases of volcanic cones. The location of volcanoes can be observed better on this map. The first phase plateau basalts and lava flows of first and second phases of volcanic cones are free of magnetic signatures. The five prominent positive magnetic anomaly enclosures are shown in Fig. 7a. These are Kula-Divlit (KUV), Kula-East (KUEV), Sandal-Divlit (SAV), Selendi (SEV), and Kaplan-Divlit (KAV), respectively. These anomalies were evaluated with the DSA algorithm and their models were presented. On the figures, cross sections were taken in the SW–NE direction of KUEV and KAV, while SAV and SEV are in the S–N direction. Finally, the cross section is taken in the W–E direction of the KUV.

To see the regional effect, upward analytic continuations were carried out at two levels ($H = 1$ km and $H = 2$ km;

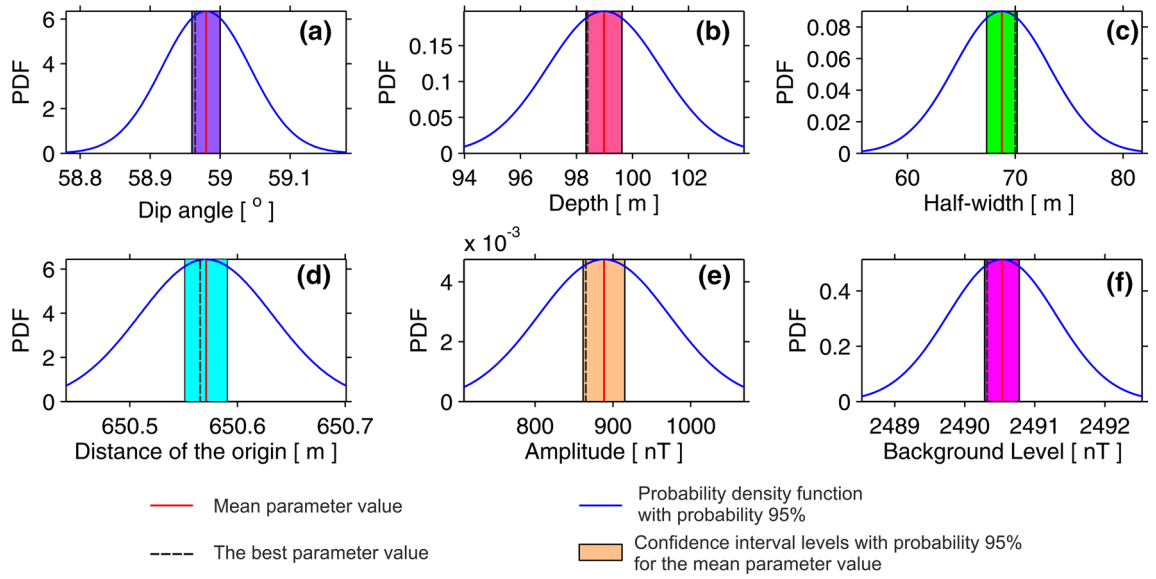

Fig. 6 Relative frequency distributions produced by using a solution set containing model parameters obtained the best runs of the DSA belong to the std of ± 30 nT case of the theoretical model

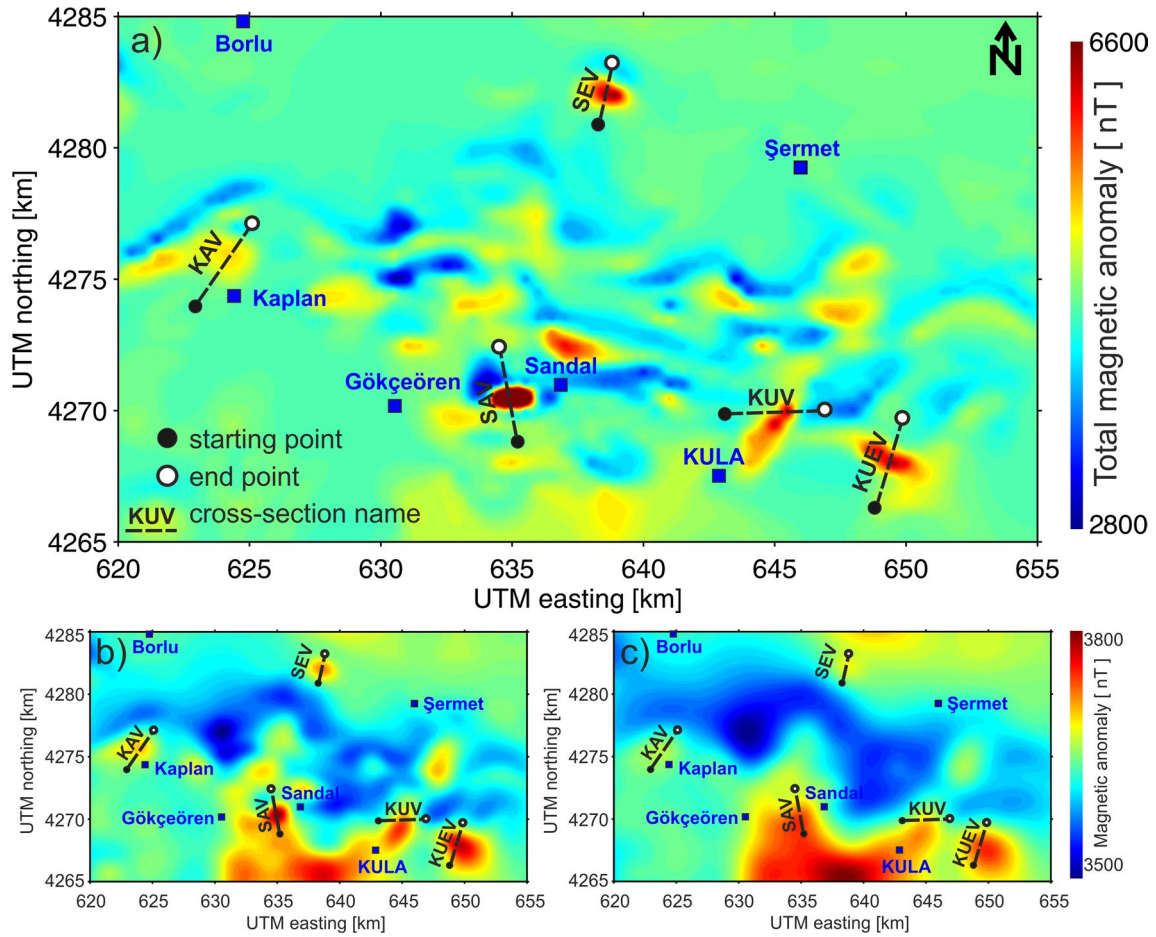

Fig. 7 **a** Aeromagnetic map of the Kula volcanic region, **b** upward continuation of the aeromagnetic map ($H = 1$ km), **c** upward continuation of the aeromagnetic map ($H = 2$ km). KUV: Kula Volcano; KUEV: Kula-East Volcano; SAV: Sandal Volcano; SEV: Selendi Volcano; KAV: Kaplan Volcano

Fig. 7b and c). The main magnetic signatures of KAV and SEV Divlits as well as the aeromagnetic anomalies at SAV, KUV, and KUEV are still very clear in the upward continuation of 1 km (Fig. 7b). However, the effects of KAV and SEV are not very obvious clear in the upward analytic continuation of 2 km (Fig. 7c). The main magnetic body is around SAV, KUV, and KUEV volcanoes.

Kula-east (KUEV)

There are signs of secondary eruption features surrounding the aeromagnetic anomaly (Fig. 8a). The length of measurement profile is 2800 m, comprising 29 data points with an interval of 100 m. The KUEV magnetic anomaly and the other four magnetic anomalies were inverted using the user-defined control parameters involving $p1 = 1$, $p2 = 5$, and a number of population (Np) of 100, max epoch (Emax) of 400. In the evaluation phase, as in the evaluation of noisy and noise-free synthetic anomalies, after 40 independent runs of DSA were performed, the solution with the lowest RMS error among these solutions was assigned as the best solution. According to the advanced evolutionary algorithm of DSA estimated dip angle, depth, half-width, distance of origin, amplitude coefficient, and background level of the dyke were found as 42.62°, 414.63 m, 472.44 m, 1465.13 m, 684.99 nT, and 3407.89 nT, with an RMS error of 8.88, respectively (Table 2). We observe that the parameter changes graphs according to the epoch number flattened after the 90th iteration and the parameter values are fixed after about 200 epochs.

Looking at the relative frequency distribution in Fig. 9, we observe that the clustering rate for all parameters is below 70% and the solution parameters are spread over a

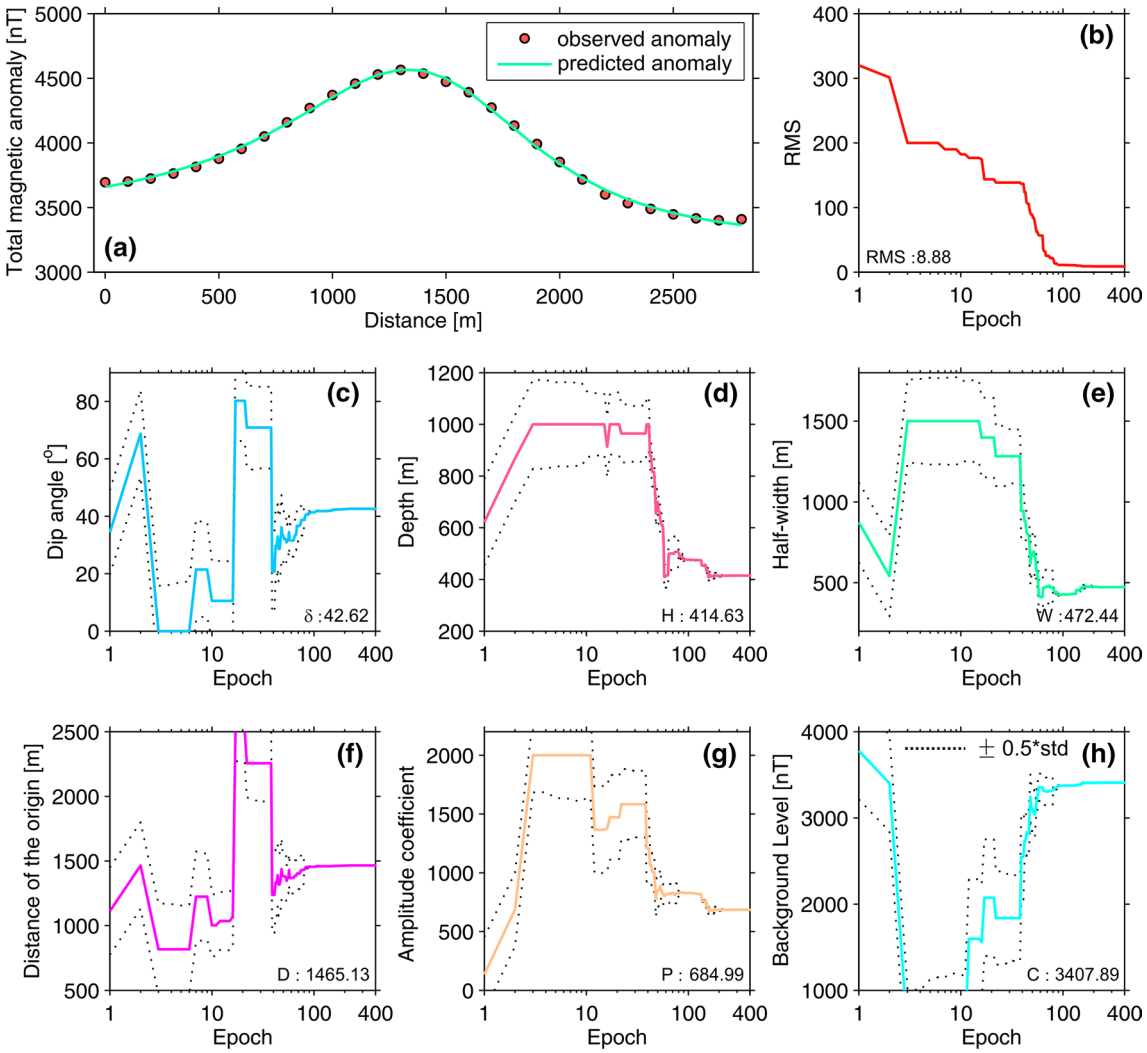

Fig. 8 **a** The comparison of the observed and predicted anomalies of KUEV, **b** Changes in the error energy with the epoch, and **c–h** present changing of model parameters at each epoch

Table 2 Statistical analyses of the best model parameter values resulted from 40 independent runs of the DSA for each model parameter of five anomalies

Statistics	δ [°]	H [m]	W [m]	D [m]	P [nT]	C [nT]	RMS
KUEV							
Search spaces	0:90	50:1000	50:1500	500:2500	100:2000	500:4000	8.88
The best	42.62	414.63	472.44	1465.13	684.99	3408.89	
Min	39.99	413.94	218.31	1446.83	683.07	3286.34	
Max	42.63	640.28	473.45	1465.31	2000.00	3408.93	
Mean	42.53	422.21	464.84	1464.89	721.81	3404.69	
Std. Dev	0.42	35.95	40.21	2.91	207.71	19.55	
SAV							
Search spaces	0:90	100:1000	50:1500	1000:3000	100:3000	2000:4000	39.86
The best	26.71	403.72	476.23	1405.03	2323.45	2411.12	
Min	26.71	191.40	476.23	1405.03	1680.29	2000.00	
Max	76.71	403.74	821.33	1996.84	2323.56	2411.28	
Mean	29.21	393.09	493.49	1434.62	2291.29	2390.56	
Std. Dev	11.04	46.93	76.17	130.63	141.96	90.74	
KUV							
Search spaces	0:90	50:1000	50:1500	500:2500	100:2000	500:4000	18.66
The best	52.34	371.99	499.99	1763.71	712.00	3291.45	
Min	52.34	274.84	499.98	1763.70	668.00	2899.52	
Max	90.00	371.99	1097.04	2476.02	712.00	3291.52	
Mean	53.28	369.54	514.92	1781.52	710.87	3281.66	
Std. Dev	5.96	15.36	94.40	112.63	6.95	61.97	
KAV							
Search spaces	0:90	100:1000	50:1500	1000:3000	100:1000	2500:4000	9.92
The best	60.99	706.44	436.19	2308.00	562.49	3434.74	
Min	0.00	324.95	420.59	1163.17	284.08	3119.40	
Max	90.00	721.97	1500.00	2826.86	593.25	3434.98	
Mean	64.53	660.26	556.17	2370.11	519.70	3413.45	
Std. Dev	15.28	98.59	257.46	279.23	91.17	55.86	
SEV							
Search spaces	0:90	100:1000	50:1500	300:1800	50:1500	500:5000	10.78
The best	33.95	452.59	456.11	1087.40	955.70	3082.23	
Min	0.00	286.59	361.30	705.15	790.90	2616.15	
Max	82.92	587.67	973.05	1800.00	1500.00	3082.43	
Mean	40.79	425.51	558.56	1192.77	937.97	955.70	
Std. Dev	21.02	68.58	204.11	295.38	110.81	178.12	

wider area in Table 3. The results for the PDF distribution with a 95% confidence interval for the best value of each model parameter are shown in Table 4. From this table, it is observed that all estimated parameters remain within the confidence intervals. Because of these results, it is an indication that the estimated parameters have good resolution.

Sandal (SAV)

This is the most outstanding volcanic cone in this region belonging to the latest phase of volcanic eruptions. Also, it gives the highest magnitude in the range of about 6500 nT (Fig. 10a). The length of measurement profile is 2500 m, comprising 26 data points with an interval of 100 m. After the total magnetic anomaly of SAV in the Sandal district has been inverted and interpreted, the estimated parameter results are presented in Table 2. These estimated parameters were found to as $\delta = 26.71°$, $H = 403.72$ m, $W = 476.23$ m, $D = 1405.03$ m, $P = 2323.45$ nT, and $C = 2411.12$ nT, with an RMS error of 39.86. It can be seen that the graph of estimated parameter change according to the number of epochs has been flattened from 30th epoch until last epoch (in Fig. 10b).

According to the relative frequency histograms shown in Figs. 11a, d, it can be observed that the δ, D parameter solutions are clustered in a narrow area and have a relative frequency value of over 80%. Because the distribution is

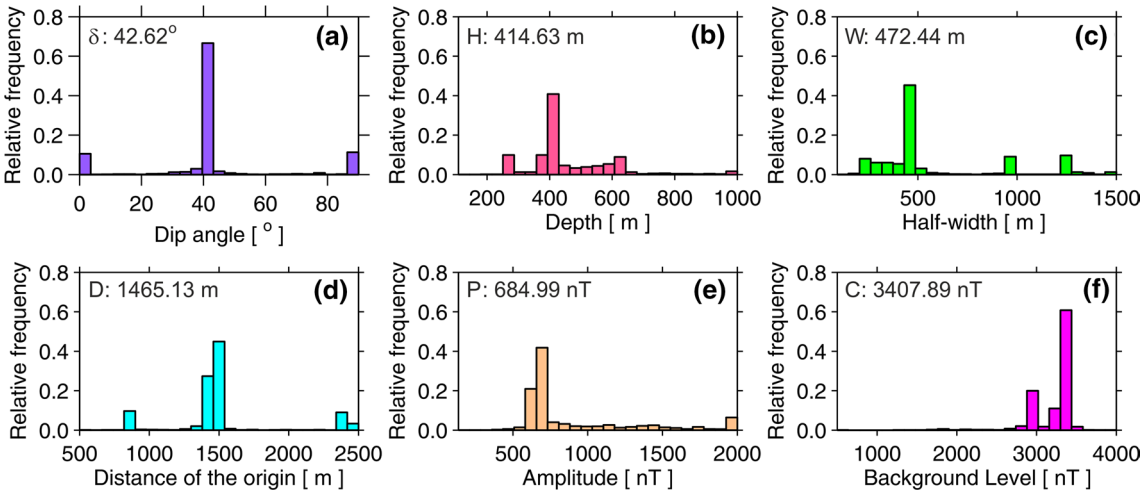

Fig. 9 Relative frequency distributions produced by using a solution set containing model parameters obtained the best runs of the DSA belong to the magnetic anomaly of KUEV

Table 3 Peak relative frequency distributions of all model parameter results belonging to the five real data obtained from the DSA and min, max, mean and std values for each parameter

Parameters	Peak relative frequency distributions (%)								
	Magnetic anomalies					Statistics			
	KUEV	SAV	KUV	KAV	SEV	Min	Max	Mean	Std. dev
δ	66.11	**87.03**	74.11	63.83	66.07	63.83	87.03	71.43	8.55
H	40.79	**66.72**	58.80	39.26	48.57	39.26	66.72	50.83	10.54
W	45.72	**76.47**	66.67	38.98	57.46	38.98	76.47	57.06	13.60
D	44.91	**88.29**	83.97	71.58	62.12	44.91	88.29	70.17	15.64
P	41.75	**66.09**	59.29	37.79	43.66	37.79	66.09	49.72	10.97
C	60.77	68.97	**70.79**	56.02	60.00	56.02	70.79	63.31	5.63

Bold values indicate maximum frequency values of parameters at magnetic anomalies

clustered in a narrow area and the frequency value is high (e.g., roughly 90% of D and δ), it is an indication that the obtained parameter results have good resolution. We observe that the remaining estimated parameters are between 60 and 70% in Table 3. For the interpretation of obtained parameters, the PDF is calculated and presented in Table 4. As shown in Table 4, the best value of each parameter is within the 95% confidence interval, indicating that the solution is good.

Kula (KUV)

Kula-Divlit (KUV) is one of the main volcanic cones of region belonging to last phase of volcanic eruptions (Ozer and Polat 2017b). It is just NE of the town of Kula. The length of measurement profile is 3000 m, comprising 31 data points with an interval of 100 m (Fig. 12a).

The analysis results obtained from DSA method are shown in Table 2. The estimated model parameters (e.g., δ, H, W, D, P, and C) are $\delta = 52.34°$, $H = 371.99$ m, $W = 499.99$ m, $D = 1763.45$ m, $P = 712.00$ nT, and $C = 3291.45$ nT, with RMS error of 18.66, respectively (Table 2). As can be seen in Fig. 12b, it is observed that the change graphs of parameter according to epoch number flatten after 60th iteration and the parameter values are fixed after about 100 epochs.

Relative frequency histograms were prepared for KUV, SEV, and KAV. However, these histograms are not shown due to the increased number of figures presented in the study. Peak relative frequency values are given in Table 4. According to the relative frequency histograms, it can be observed that the δ, D, and C parameter solutions are clustered in a narrow area and have a relative frequency value of over 70%. Because the distribution is clustered in a narrow area and the frequency value is high (e.g., roughly 85% of D and δ of 78%) in Table 3, it is an indication that the obtained parameter results have good resolution. The other parameters, especially H, P, and W, have relatively lower resolution due to their wider dispersion and below 70%. For the

Table 4 Statistical analyses of the best model parameter values resulted from 40 independent runs of the DSA and lower and upper bounds obtained from PDFs at 95% confidence intervals for each model parameter of five anomalies

Statistics	δ [°]	H [m]	W [m]	D [m]	P [nT]	C [nT]
KUEV						
The best	42.62	414.63	472.44	1465.13	684.99	3408.89
Mean	42.53	422.21	464.84	1464.49	721.81	3404.69
Lower bound	42.39	410.71	451.98	1463.56	655.38	3398.44
Upper bound	42.66	433.71	477.69	1465.42	788.24	3410.95
SAV						
The best	26.71	403.72	476.23	1405.03	2323.45	2411.12
Mean	29.21	393.09	493.49	1434.62	2291.29	2390.56
Lower bound	25.68	378.08	469.13	1392.85	2245.89	2361.54
Upper bound	32.74	408.09	517.85	1476.40	2336.69	2419.59
KUV						
The best	52.34	371.99	499.99	1763.71	712.00	3291.45
Mean	53.28	369.54	514.92	1781.52	710.87	3281.66
Lower bound	51.37	364.63	484.73	1745.50	708.65	3261.84
Upper bound	55.18	374.45	545.11	1817.54	713.09	3301.48
KAV						
The best	60.99	**706.44**	**436.19**	2308.00	**562.49**	**3434.74**
Mean	64.53	660.26	556.17	2370.11	519.70	3413.45
Lower bound	59.65	628.73	473.83	2280.81	490.55	3395.58
Upper bound	69.42	691.79	638.51	2459.42	548.86	3431.31
SEV						
The best	**33.95**	**452.59**	**456.11**	**1087.40**	955.70	**3082.23**
Mean	40.79	425.51	558.56	1192.77	937.97	2984.04
Lower bound	34.07	403.58	493.28	1098.30	902.53	2927.08
Upper bound	47.51	447.44	623.83	1287.23	973.41	3041.00

Bold values indicate model parameters that are outside of 95% confidence intervals

interpretation of obtained parameters, the PDF is calculated and presented in Table 4. As shown in Table 4, the best value of each parameter is within the 95% confidence interval, indicating that the solution is good. This result suggests that the main sub-volcanic body is not reached the surface, and the resulting extensive lava flows may have been connected by thin feeder dykes with main sub-volcanic body.

Kaplan (KAV)

This volcanic cone is at the western end of Kula volcanic region placed on the eastern side. There are two volcanic eruption centers over this volcano. The amplitude of this anomaly is about 4000 nT. The extension of this anomaly can be followed in the WSW direction.

The length of measurement profile is 3300 m, comprising 34 data points with an interval of 100 m (Fig. 12c). The total magnetic anomaly of KAV in Kaplan district, located in the westernmost part of study area, was interpreted and the estimated parameter results are presented in Table 2. These estimated parameters were found to $\delta = 60.99°$, $H = 706.44$ m, $W = 436.11$ m, $D = 2308.00$ m, $P = 562.49$ nT, and $C = 3474.74$ nT, with an RMS error of 9.92. It can be seen that the graph of estimated parameter change according to the number of epochs has been flattened from 55th epoch until last epoch (in Fig. 12d).

When relative frequency histograms of these evaluation results are examined, it was observed that the dip angle and distance of origin are roughly around 60%, while the remaining parameters are spread between 40 and 60% (in Table 3). Simultaneously, the subplots show that the solutions for all parameters are more widely spread. As shown in Table 4, except for δ and D, the others are just outside the 95% confidence interval. It can be said that the PDF distribution and the relative frequency distribution are compatible.

Selendi (SEV)

There is no obvious sign of a volcanic cone, but there is a compelling aeromagnetic anomaly at a magnitude of about 4520 nT. This magmatic body has probably unreached the surface therefore there is no cinder cone. This magmatic intrusion is probably caused by the bend in course of ancient river. The length of measurement profile is

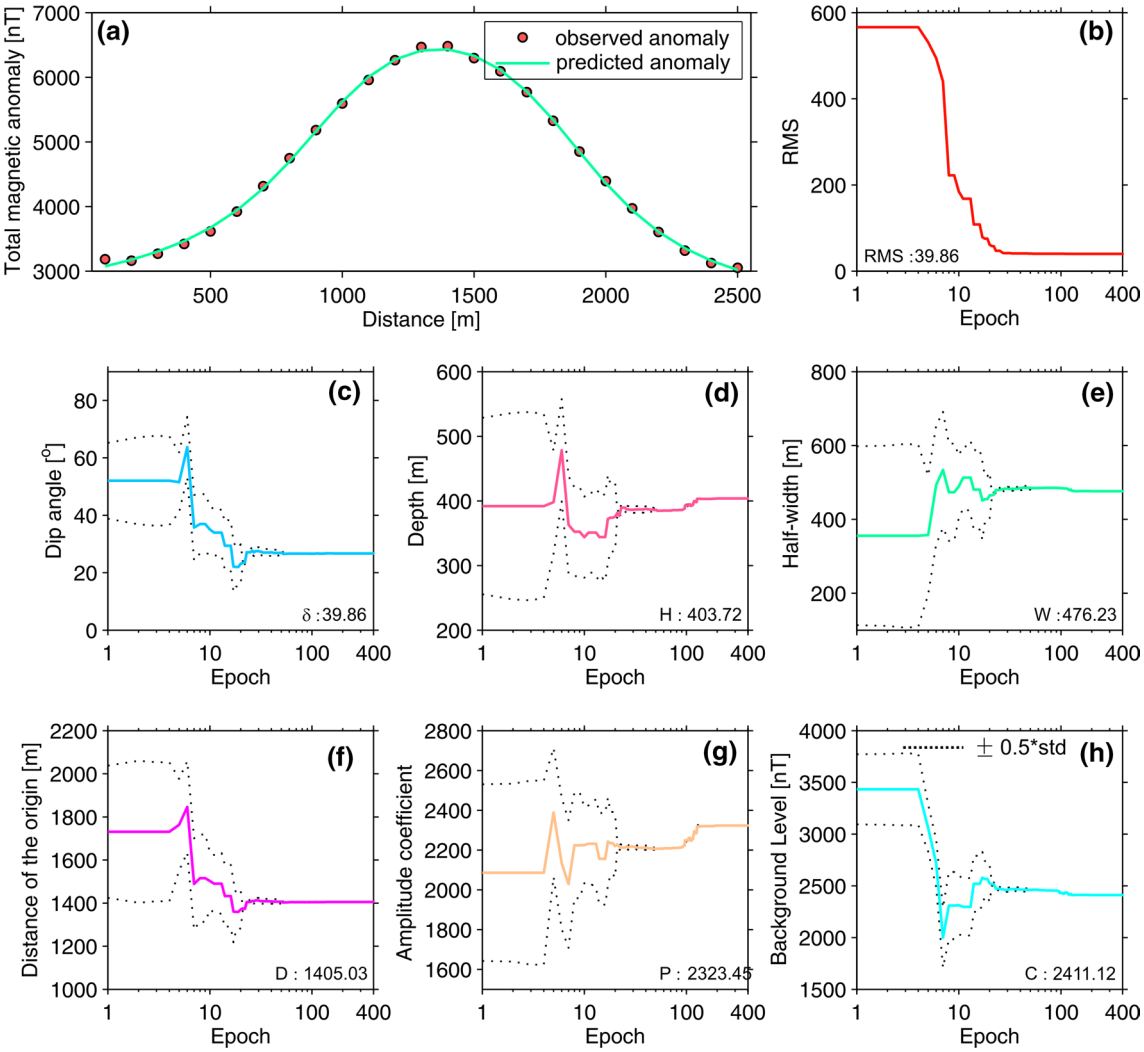

Fig. 10 **a** The comparison of the observed and predicted anomalies of SAV, **b** Changes in the error energy with the epoch, and **c–h** present changing of model parameters at each epoch

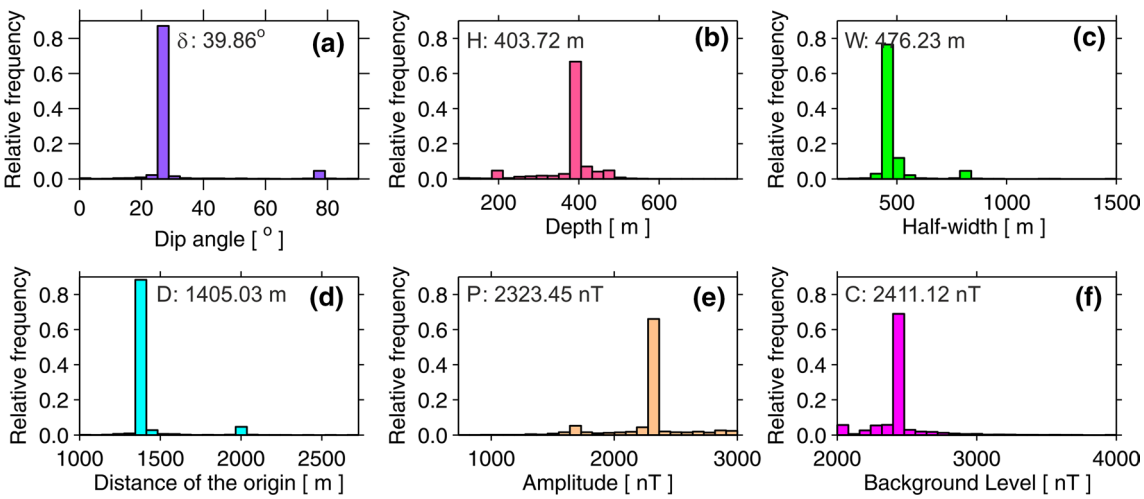

Fig. 11 Relative frequency distributions produced by using a solution set containing model parameters obtained the best runs of the DSA belong to the magnetic anomaly of SAV

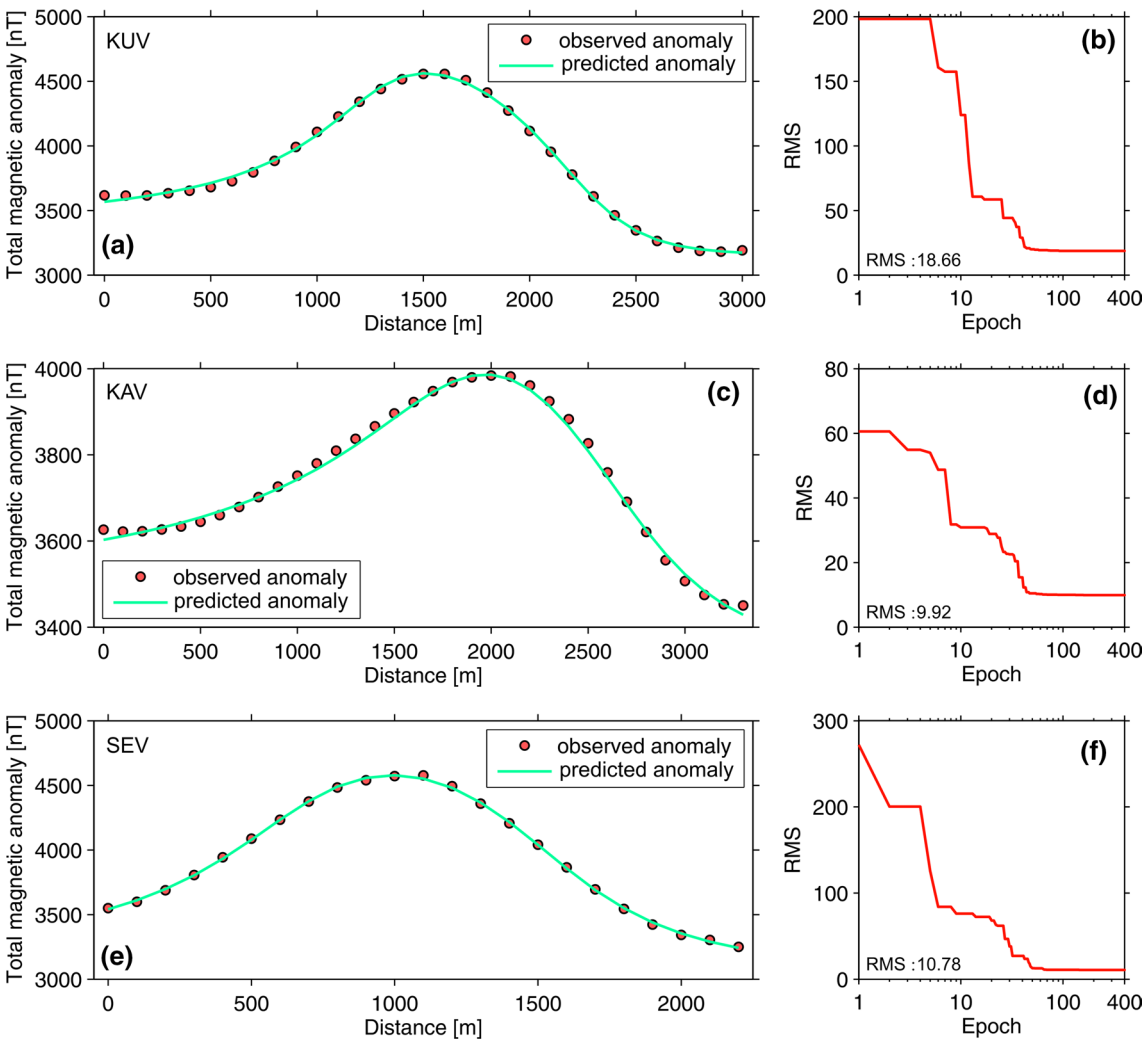

Fig. 12 **a** The comparison of the observed and predicted anomalies of KUV; **b** Changes in the error energy of KUV with the epoch; **c** the comparison of the observed and predicted anomalies of KAV; **d** Changes in the error energy of KAV with the epoch; **e** the comparison of the observed and predicted anomalies of SEV; **f** Changes in the error energy of SEV with the epoch

2200 m, comprising 23 data points with an interval of 100 m (Fig. 12e).

The total magnetic anomaly of the SEV in the Selendi region, located in the northernmost part of study area, was interpreted and the estimated parameter results are presented in Table 2. These estimated parameters were found as $\delta = 33.95°$, $H = 452.59$ m, $W = 456.11$ m, $D = 1087.40$ m, $P = 955.70$ nT, and $C = 3082.23$ nT, with an RMS error of 10.78. It can be seen that the graph of the estimated parameter change according to the number of epochs has been flattened from the 70th epoch until the last epoch (in Fig. 12f). According to the relative frequency histograms of these evaluation results, we observe that dip angle and distance of origin are roughly around 70%, while the remaining parameters are spread between 40 and 60% in Table 3. Simultaneously, the subplots show that the solutions for all parameters are more widely spread. As shown in Table 4, except for the amplitude coefficient (P), the others are just outside the 95% confidence interval. It can be said that the PDF distribution and the relative frequency distribution are compatible.

Results

To test the efficiency of DSA algorithm, which is one of the innovative metaheuristic optimization method, inversion operations were carried out first on the theoretical model without noise and then on the theoretical models with different noise levels. Then, an inverse modeling study was applied to real field data. The five obvious magnetic anomalies of Kula volcanoes were solved with this algorithm. 40 independent runs were performed to ensure neutrality and

to determine the accuracy and efficiency of the results from the inversion. The results of synthetic anomaly demonstrated that the acquired 2D dipping dayk model parameters were close to the actual values for both cases.

Aeromagnetic data for the Kula volcanic field were integrated to describe the state of subsurface structures of area. They commonly display marked magnetic anomaly contrast in accordance with the surrounding rocks, which are composed of sedimentary and metamorphic rocks. While all of the model parameter values of the KUEV, SAV, and KUV anomalies remain within the 95% confidence interval, it is seen that some of the model parameter values of KAV and SEV anomalies are just outside the 95% confidence interval but very close to the bounds. According to the results of the PDFs, the fact that most of the parameters are within a narrow confidence interval is an indicator of the effectiveness of the method. According to the results of the upward continuation made, it was shown that the main source causing the magnetic anomaly was located in the south of study area. Although the KAV and the SEV are not obvious because of upward continuation, three positive anomalies, namely the SAV, the KUV, and the KUEV volcanoes, are evident in the southern part of study area.

The depths of dyke model can be listed as 371.99 m, 414.63 m, 403.72 m, 452.59 m, and 706.44 m for the five areas (e.g., KUV, KUEV, SAV, SEV, and KAV, respectively). Except for the KAV magnetic anomaly, the others are close to each other in Table 5. The minimum, maximum, mean, and std of the estimated depths for the five areas were 371.99 m, 706.44 m, 469.87 m, and 121.06 m, respectively. This result suggests that the main sub-volcanic body is not reached the surface, and that the resulting extensive lava flow may have been connected by thin feeder dykes with the main sub-volcanic body.

We investigated the relative frequency distribution in the estimated parameter solutions and found 58.80%, 40.79%, 66.72%, 48.57%, and 39.26% for the depths of dyke to upper surface, respectively. The minimum, maximum, mean, and std of values of the relative frequency distributions for the estimated depths of anomalies are 39.26%, 66.72% m, 50.83%, and 10.54%, respectively.

While the depth values of KUV, KUEV, and SAV anomalies remain within the 95% confidence interval, it is seen that the depths of KAV and SEV anomalies are just outside the 95% confidence interval but very close to the bounds.

Secondly, we can list the half-width as 499.99 m, 472.44 m, 476.23 m, 456.11 m, and 436.19 m. The half-width values are very close to each other. The minimum, maximum, mean, and std of the estimated depths were 436.19 m, 499.99 m, 468.19 m, and 21.28 m, respectively. We also investigated the relative frequency distribution in the estimated parameter solutions and found 66.67%, 45.72%, 76.47%, 57.46%, and 39.98% for the half-width of dyke, respectively. Among these values, the best relative frequency value (e.g., 76.47%) belongs to the SAV data. The average relative frequency value of 6 estimated parameters of all field data is 60.42%.

The amplitude coefficient of SAV data draws attention compared with the others. From this viewpoint, we can say that the susceptibility contrast is high compared to the surrounding rocks, which are sedimentary and metamorphic rocks. When the base levels are averaged, it can be said that the mean value for the region is roughly 2323 nT.

Conclusions

The applicability and efficiency of DSA technique are convincing for its application to total magnetic anomalies acquired in a volcanic area. Both synthetic model and field data evaluation results as well as statistical test results revealed the success of model parameter estimations. Outcomes showed that potential field methods were successful in imaging underground structures by resembling Kula volcanoes to dyke-shaped structures.

The 2D structural model obtained from the cross section data of this study is credible as a first input for the subsequent analysis and can be improved by performing 3D modeling studies in future. Research that covers model parameter estimations for magnetic anomalies and drilling information is not widely available. For this reason, the parameter results estimated with the help of DSA technique can be further enhanced by new geophysical research, and compared with

Table 5 The best model parameter values belonging to the five real data

Parameters		Best model parameter values of magnetic anomalies				
		KUEV	SAV	KUV	KAV	SEV
Dip angle	δ [°]	42.62	26.71	52.34	60.99	33.95
Depth	H [m]	414.63	403.72	371.99	706.44	452.59
Half-width	W [m]	472.44	476.23	499.99	436.19	456.11
Distance from the origin	D [m]	1465.13	1405.03	1763.71	2308.00	1087.40
Amplitude coefficient	P [nT]	684.99	2323.45	712.00	562.49	955.70
Background level	C [nT]	3408.89	2411.12	3291.45	3434.74	3082.23

parameter results of any other study. The usage of map data can also be considered instead of cross sections.

As a result, it is worth mentioning that the technique used in this study is recommended to interpret the magnetic anomalies in volcanic areas and to characterize the form of dyke-shaped magnetic intrusions in the crust. This work is constituted as a contribution to this knowledge of the DSA algorithm.

Appendix. Inversion steps

Step (1) Set user-defined and control parameters: setting *Np, G, p*1, *p*2, and threshold (*t_hold*)

In this stage, setting of control parameters such as the number of superorganisms (*Np*), generation (*G*), and control parameters (*p*1*, p*2) are defined ($p_1 = p_2 = \mathrm{SF}\ x\ \mathrm{rand}_{1,2}$, SF = 0.3).

Step (2) Initialize the artificial organism: calculating $x_{i,j}$ using Eq. (1)

This step shows that the initial position of organism in search space is randomly generated using the equation $x_{i,j} = x_j^{\mathrm{low}} + \mathrm{rand}_{i,j} \times \left(x_j^{\mathrm{up}} - x_j^{\mathrm{low}}\right)$, where $\mathrm{rand}_{\mathrm{i,j}}$ is a uniformly distributed random number between 0 and 1, x_j^{low} and x_j^{up} represent the lower and upper limits of organism location.

Step (3) Random shuffling superorganism and determining scale value: determining donor targets and scale value

In this stage, randomly selected individuals of the superorganism identified in the previous stage are determined by the scale factor, the degree of movement toward the donor's targets to discover the stopover site. The size of change in positions of members of superorganism is controlled by the scale value, which can be produced by gamma, normal, or lognormal random number generator. The values of scale are given by the equation Scale = rand*g* (2 *x* rand_1) *x* rand_2 *x* rand_3, where rand_1, rand_2, and rand_3 are uniformly distributed random numbers between 0 and 1. The rand*g* is a random number generator.

Step (4) Determine the stopover site: calculating $S_{i,G}$ using Eq. (2)

At this stage, the stopover sites are determined by the Brownian-like random-walk model. Randomly chosen organisms move toward targets represented by the donor. The equation $s_{i,G} = X_{i,G} + \mathrm{scale} \times \left(\mathrm{donor} - X_{i,G}\right)$ is used to find the stopover site, where $\mathrm{donor} = X_{\mathrm{random\_shiffling}}$.

Step (5) Check the bounds of stopover site: Check $x_j^{\mathrm{low}} \le S_j \le x_j^{\mathrm{up}}$

x_j^{low} and x_j^{up} represent the lower and upper limits of organism location. It is checked whether the location of each organism in the stopover site remains within the predefined search space. If it falls outside, locations are drawn to these limits.

Step (6) Determine the trial vector: calculating $S^*_{i,j,k}$ using Eq. (3)

If the new stopover site is better than the current location, superorganism moves to the new stopover site. This new stopover site is identified by the equation $S^*_{i,j,G} = \begin{cases} S_{i,j,G} \\ X_{i,j,G} \end{cases} \text{if} \begin{cases} \mathrm{rand}_{i,j} = 0 \\ \mathrm{rand}_{i,j} = 1 \end{cases}$.

Step (7) Choose the next generation: calculating $X_{i,G+1}$ using Eq. (4)

At this stage, if the trial vector provides an error value which is equal or less than the target vector, it changes the target vector in the next epoch. Otherwise, its current position is retained. This target vector is identified by the equation $X_{i,G+1} = \begin{cases} S_{i,G} \\ X_{i,G} \end{cases} \text{if} \begin{cases} f\left(S^*_{i,G}\right) \le f\left(X_{i,G}\right) \\ \text{otherwise} \end{cases}$.

Step (8) Data misfit: calculating RMS using Eq. (5)

In iterative inversion methods, it is important to stop the iterative process at an optimal number of iterations. The stopping criteria for terminating iteration in MI methods are based on the misfit between the observed data and the predicted data. At this stage, the data misfit is made with the equation $\mathrm{RMS} = \sqrt{\frac{1}{N}\sum_{k=1}^{N}\left(d_k^{\mathrm{obs}} - d_k^{\mathrm{cal}}\right)^2}$.

Step (9) Stopping criteria:

If this data misfit is equal or greater than the threshold value or the epoch number less than the predefined max epoch number (G_{max}), the loop between steps (3) and (9) continues. Otherwise, the algorithm is terminated.

Acknowledgements I am grateful to the General Directorate of Mining Research and Exploration (MTA) of Türkiye for the aeromagnetic data. I sincerely thank Prof. Dr. Mustafa Ergun from Dokuz Eylul University, İzmir (Türkiye) for his valuable and helpful comments. I also thank Prof. Dr. from Hasan Sözbilir Dokuz Eylul University, İzmir (Türkiye) for his comments and contributions to the geology of the region. I want to thank Ph.D. Ray Cakir, Senior Scientist (Geological Hazards) at WADNR-Washington Geological Survey, for his suggestions. This paper is greatly enhanced by the comments of Colin Farquharson and an anonymous reviewer.

Declarations

Conflict of interest The author declares that he has no competing interests.

References

Abdelrahman ESM, Abo-Ezz ER, Essa KS (2012) Parametric inversion of residual magnetic anomalies due to simple geometric bodies. Explor Geophys 43:178–189. https://doi.org/10.1071/EG11026

Al-Garni MA (2015) Interpretation of magnetic anomalies due to dipping dikes using neural network inversion. Arab J Geosci 8:8721–8729. https://doi.org/10.1007/s12517-014-1770-7

Alkan H, Balkaya Ç (2018) Parameter estimation by differential search algorithm from horizontal loop electromagnetic (HLEM) data. J Appl Geophys 149:77–94. https://doi.org/10.1016/j.jappgeo.2017.12.016

Anderson NL, Essa KS, Elhussein M (2020) A comparison study using particle swarm optimization inversion algorithm for gravity anomaly interpretation due to a 2D vertical fault structure. J Appl Geophys 179:104120. https://doi.org/10.1016/j.jappgeo.2020.104120

Ateş A, Kearey P, Tufan S (1999) New gravity and magnetic anomaly maps of Turkey. Geophys J Int 136:499–502. https://doi.org/10.1046/j.1365-246X.1999.00732.x

Balkaya Ç, Ekinci YL, Göktürkler G, Turan S (2017) 3D non-linear inversion of magnetic anomalies caused by prismatic bodies using differential evolution algorithm. J Appl Geophys 136:372–386. https://doi.org/10.1016/j.jappgeo.2016.10.040

Balkaya Ç, Kaftan I (2021) Inverse modelling via differential search algorithm for interpreting magnetic anomalies caused by 2D dyke-shaped bodies. J Earth Syst Sci. https://doi.org/10.1007/s12040-021-01614-1

Barbosa VCF, Silva JBC (1997) Medeiros WE (1997) gravity inversion of basement relief stabilized by equality constraints on depth. SEG Annu Meet 6:470–473. https://doi.org/10.1190/1.1885935

Beiki M, Pedersen LB (2012) Estimating magnetic dike parameters using a non-linear constrained inversion technique: an example from the Sarna area, westcentral Sweden. Geophys Prospect. https://doi.org/10.1111/j.1365-2478,2011.01010.x

Bhimasankaram VLS, Mohan NL, Rao SVS (1978) Interpretation of magnetic anomalies of dikes using Fourier transforms. Geoexploration 16:259–266. https://doi.org/10.1016/0016-7142(78)90015-7

Bilim F (2007) Investigations into the tectonic lineaments and thermal structure of Kutahya-Denizli region, western Anatolia, from using aeromagnetic, gravity and seismological data. Phys Earth Planet Inter 165:135–146. https://doi.org/10.1016/j.pepi.2007.08.007

Bilim F, Akay T, Aydemir A, Kosaroglu S (2016) Curie point depth, heat-flow and radiogenic heat production deduced from the spectral analysis of the aeromagnetic data for geothermal investigation on the Menderes Massif and the Aegean Region, western Turkey. Geothermics 60:44–57. https://doi.org/10.1016/j.geothermics.2015.12.002

Biswas A, Acharya T (2016) A very fast simulated annealing method for inversion of magnetic anomaly over semi-infinite vertical rod-type structure. Model Earth Syst Environ 2:1–10. https://doi.org/10.1007/s40808-016-0256-x

Biswas A, Parija MP, Kumar S (2017) Global nonlinear optimization for the interpretation of source parameters from total gradient of gravity and magnetic anomalies caused by thin dyke. Ann Geophys. https://doi.org/10.4401/ag-7129

Candan O, Dora O, Oberhänsli R, Çetinkaplan M, Partzsch JH, Friederike CW, Dürr S (2001) Pan-African high-pressure metamorphism in the Precambrian basement of the Menderes Massif, western Anatolia, Turkey. Int J Earth Sci 89:793–811. https://doi.org/10.1007/s005310000097

Chen CS (1999) TEM Investigations of aquifers in southwest coast of Taiwan. Ground Water 37:890–893

Civicioglu P (2012) Transforming geocentric cartesian coordinates to geodetic coordinates by using differential search algorithm. Comput Geosci 46:229–247. https://doi.org/10.1016/j.cageo.2011.12.011

Constable SC, Parker KL, Constable CG (1987) Occam's inversion a practical algorithm for generating smooth models from EM sounding data. Geophysics 52:289–300

Cooper GRJ (2012) The semi-automatic interpretation of magnetic dyke anomalies. Comput Geosci 44:95–99. https://doi.org/10.1016/j.cageo.2012.02.016

Dolmaz MN, Hisarli ZM, Ustaömer T, Orbay N (2005) Curie point depths based on spectrum analysis of aeromagnetic data, West Anatolian extensional province, Turkey. Pure Appl Geophys 162:571–590. https://doi.org/10.1007/s00024-004-2622-2

Dorigo M (1992) Optimization, learning and natural algorithms. PhD thesis, Dipartimento di Elettronica, Politecnico di Milano, Milan, Italie

Di MR, Milano L, Piegari E, Milano L (2020) Modeling of magnetic anomalies generated by simple geological structures through genetic-price inversion algorithm. Phys Earth Planet Inter 305:106520. https://doi.org/10.1016/j.pepi.2020.106520

Ekinci YL, Balkaya Ç, Göktürkler G (2019) Parameter estimations from gravity and magnetic anomalies due to deep-seated faults : differential evolution versus particle swarm optimization. Turkish J Earth Sci. https://doi.org/10.3906/yer-1905-3

Ekinci YL, Balkaya Ç, Göktürkler G, Özyalın Ş (2021) Gravity data inversion for the basement relief delineation through global optimization: a case study from the Aegean Graben System, western Anatolia, Turkey. Geophys J Int 224:923–944. https://doi.org/10.1093/gji/ggaa492

Ekinci YL, Balkaya Ç, Göktürkler G, Turan S (2016) Model parameter estimations from residual gravity anomalies due to simple-shaped sources using differential evolution algorithm. J Appl Geophys 129:133–147. https://doi.org/10.1016/j.jappgeo.2016.03.040

Ekinci YL, Özyalın Ş, Sındırgı P, Balkaya Ç, Göktürkler G (2017) Amplitude inversion of the 2D analytic signal of magnetic anomalies through the differential evolution algorithm. J Geophys Eng 14:1492–1508. https://doi.org/10.1088/1742-2140/aa7ffc

Eppelbaum LV (2015) Quantitative interpretation of magnetic anomalies from bodies approximated by thick bed models in complex environments. Environ Earth Sci 74:5971–5988

Erbek E (2021) An investigation on the structures and the basement depth estimation in the western Anatolia, Turkey using aeromagnetic data. Geosci J 25:891–902. https://doi.org/10.1007/s12303-021-0001-y

Essa KS, Elhussein M (2017) A new approach for the interpretation of self-potential data by 2-D inclined plate. J Appl Geophys 136:455–461. https://doi.org/10.1016/j.jappgeo.2016.11.019

Farquharson CG (2008) Constructing piecewise-constant models in multidimensional minimum-structure inversions. Geophysics 73(1):K1–K9. https://doi.org/10.1190/1.2816650

Gessner K, Gallardo LA, Wedin F, Şener K (2016) Crustal structure of the northern Menderes Massif, western Turkey, imaged by joint gravity and magnetic inversion. Int J Earth Sci 105:2133–2148. https://doi.org/10.1007/s00531-016-1324-1

Gobashy M, Abdelazeem M (2020) Minerals and ore deposits exploration using meta-heuristic based optimization. Contrib Geophys Geod 50:161–199. https://doi.org/10.31577/congeo.2020.50.2.1

Holland JH (1975) Adaptation in natural and artificial systems. University of Michigan Press, Ann Arbor, MI

Kaftan I (2017) Interpretation of magnetic anomalies using a genetic algorithm. Acta Geophys 65:627–634. https://doi.org/10.1007/s11600-017-0060-7

Kara I (1997) Magnetic interpretation of two-dimensional dikes using integration-nomograms. J Appl Geophys 36:175–180. https://doi.org/10.1016/S0926-9851(96)00054-7

Karaboğa D (2005) An idea based on honey bee swarm for numerical optimization, Technical report-TR06. Erciyes University, Engineering Faculty, Computer Engineering Department

Keating P, Pilkington M (2004) Euler deconvolution of the analytic signal and its application to magnetic interpretation. Geophys Prospect 52:165–182

Kennedy J, Eberhart RC (1995) Particle swarm optimization. Proceedings of the IEEE Int Conf Neural Netw 4:1942–1948

Li Y, Oldenburg DW (1996) 3-D inversion of magnetic data. Geophysics 61:394–408. https://doi.org/10.1190/1.1443968

Marquardt D (1963) An algorithm for least-squares estimation of nonlinear parameters. SIAM J Appl Math 11:431–441. https://doi.org/10.1137/0111030

Mohan NL, Sundararajan N, Rao SVS (1982) Interpretation of some two-dimensional magnetic bodies using Hilbert transforms. Geophysics 47:376–387

Murthy IVR (1985) The midpoint method: magnetic interpretation of dikes and faults. Geophysics 50:834–839

MTA (1962) Mineral Research and Exploration Institute (MTA) of Turkey

Omran MGH, Clerc M (2011) http://www.particleswarm.info/ .Last Accessed 19 Sep 2022

Otis GW (2004) Sociality of insects. In: Encyclopedia of entomology. Springer, Dordrecht. https://doi.org/10.1007/0-306-48380-7_3965

Ozer C, Polat O (2017) 3-D crustal velocity structure of Izmir and surroundings. J Fac Eng Archit Gazi Univ 32(3):733–748. https://doi.org/10.17341/gazimmfd.337620

Ozer C, Polat O (2017b) Local earthquake tomography of Izmir geothermal area, Aegean region of Turkey. Boll Geofis Teor Appl 58:17–42. https://doi.org/10.4430/bgta0191

Pujol J (2007) The solution of nonlinear inverse problems and the Levenberg–Marquardt method. Geophysics 72:1–16

Ram Babu HV, Rao Atchuta D (1991) Application of the Hilbert transform for gravity and magnetic interpretation. Pure Appl Geophys PAGEOPH 135:589–599. https://doi.org/10.1007/BF01772408

Rao DA, Ram Babu HV (1981) Nomograms for rapid evaluation of magnetic anomalies over long tabular bodies. Pure Appl Geophys PAGEOPH 119:1037–1050. https://doi.org/10.1007/BF00878968

Reid AB, Allsop JM, Granser H, Millett AJ, Somerton IW (1990) Magnetic interpretation in three dimensions using Euler deconvolution. Geophysics 55:80–91

Salem A, Ravat D, Smith R, Ushijima K (2005) Interpretation of magnetic data using an enhanced local wavenumber (ELW) method. Geophysics 70(2):7–12

Song X, Li L, Zhang X, Huang J, Shi X, Jin S, Bai Y (2014) An implementation of differential search algorithm (DSA) for inversion of surface wave data. J Appl Geophys 111:334–345. https://doi.org/10.1016/j.jappgeo.2014.10.017

Sözbilir H (2002) Geometry and origin of folding in the neogene sediments of the gediz graben, western Anatolia. Turk Geodin Acta 15(5–6):277–288. https://doi.org/10.1016/S0985-3111(02)01093-8

Spies BR, Macnae JC (1997) Electromagnetic trends – spatial, temporal and economic, pp 489 – 496. In: Proceedings of exploration 97, fourth decennial international conference on mineral exploration, AG Gubins (ed), Prospectors and Developers Association of Canada, p 1068

Srivastava S, Agarwal BNP (2010) Inversion of the amplitude of the two-dimensional analytic signal of the magnetic anomaly by the particle swarm optimization technique. Geophys J Int 182:652–662. https://doi.org/10.1111/j.1365-246X.2010.04631.x

Stampolidis A, Tsokas GN (2012) Use of edge delineating methods in interpreting magnetic archaeological data. Archaeol Prospect 19:123–140

Storn R, Price K (1995). Differential evolution – a simple and efficient adaptive scheme for global optimization over continuous spaces. Technical Report TR-95-012. International Computer Science Institute, Berkeley, USA.

Şekercioğlu CH (2007) Conservation ecology: area trumps mobility in fragment bird extinctions. Curr Biol. https://doi.org/10.1016/j.cub.2007.02.019

Tarantola A (2005) Inverse problem theory and methods for model parameter estimation. SIAM, Philadelphia, p p358

Tokçaer M, Agostini S, Savaşçin MY (2005) Geotectonic setting and origin of the youngest Kula volcanics (western Anatolia), with a new emplacement model. Turk J Earth Sci 14:145–166

Trianni V, Tuci E, Passino KM, Marshall JAR (2011) Swarm cognition: an interdisciplinary approach to the study of self-organising biological collectives. Swarm Intell 5:3–18. https://doi.org/10.1007/s11721-010-0050-8

Venkata Raju DC (2003) LIMAT: a computer program for least-squares inversion of magnetic anomalies over long tabular bodies. Comput Geosci 29:91–98. https://doi.org/10.1016/S0098-3004(02)00108-5

Won IJ (1981) Application of Gauss's method to interpretation of magnetic anomalies of dipping dikes. Geophysics 46:211–215

Yang XS, Deb S (2009) Cuckoo search via L´evy flights. In: IEEE world congress on nature and biologically inspired computing (NaBIC) Coimbatore, India, pp 210–214